January 2014

Investigating The Effects Of Ocean Bubbles On Enhanced Aqua-MODIS Aerosol Optical Depth Retrievals In The Mid-To-High Latitude Southern Oceans

Matt Christensen

Follow this and additional works at: https://commons.und.edu/theses

Recommended Citation

INVESTIGATING THE EFFECTS OF OCEAN BUBBLES ON ENHANCED AQUA-MODIS
AEROSOL OPTICAL DEPTH RETRIEVALS IN THE MID-TO-HIGH LATITUDE
SOUTHERN OCEANS

By

Matt Christensen

Bachelor of Science, University of North Dakota, 2011

A Thesis

Submitted to the Graduate Faculty

Of the

University of North Dakota

In partial fulfillment of the requirements

For the degree of

Master of Science

Grand Forks, North Dakota
August
2014

This thesis, submitted by Matt Christensen in partial fulfillment of the requirements for the Degree of Master of Science from the University of North Dakota, has been read by the Faculty Advisory Committee under whom the work has been done and is hereby approved.

_____
Dr. Jianglong Zhang, Chairperson

_____
Prof. Michael R. Poellot, Committee Member

_____
Dr. Edward Hyer, Committee Member

This thesis is being submitted by the appointed advisory committee as having met all of the requirements of the School of Graduate Studies at the University of North Dakota and is hereby approved.

_____
Dr. Wayne Swisher
Dean, School of Graduate Studies

_____
Date

PERMISSION

Title   Investigating the Effects of Ocean Bubbles on Enhanced Aqua MODIS Aerosol Optical Depth Retrievals in the Mid-to-High Latitude Southern Oceans

Department   Atmospheric Sciences

Degree   Master of Science

In presenting this thesis in partial fulfillment of the requirements for a graduate degree from the University of North Dakota, I agree that the library of this University shall make it freely available for inspection. I further agree that permission for extensive copying for scholarly purposes may be granted by the professor who supervised my thesis work or, in their absence, by the chairperson of the department or the dean of the School of Graduate Studies. It is understood that any copying or publication or other use of this thesis or part thereof for financial gain shall not be allowed without my written permission. It is also understood that due recognition shall be given to me and to the University of North Dakota in any scholarly use which may be made of any material in my thesis.

Matt Christensen

7/10/2014

TABLE OF CONTENTS

LIST OF FIGURES

ACKNOWLEDGEMENTS

I would like to thank my advisor Dr. Jianglong Zhang and also my committee members Prof. Michael R. Poellot and Dr. Edward Hyer for the guidance given to me throughout this thesis work and all my schooling. I thank Dr. Xiaodong Zhang for helping me in getting this project started. A special thank you to the Atmospheric Science Department for everything it has done for me since I arrived at UND. Thank you to family and friends, who have all been supportive in ways they can't imagine.

ABSTRACT

While satellite remote sensing aerosol measurements are widely used for climate, visibility and air quality studies, issues exist in the current satellite aerosol products such as the Elevated Southern Oceans Anomaly (ESOA) phenomenon. The ESOA is an elevated aerosol optical depth (AOD) belt over high latitude southern oceans detected by passive satellites such as the Moderate Resolution Imaging Spectroradiometer (MODIS) and Multi-angle Imaging SpectroRadiometer (MISR). The ESOA feature, however, is not present in the ground based studies. Cloud contamination was found to have a significant impact on this anomaly, but it is not the only contributor. Wind generated ocean bubbles could increase ocean surface reflectance. However, oceanic bubbles have not been considered in the conventional satellite aerosol studies. In this study, the effects of oceanic bubbles on satellite retrieved AOD values are studied using the linked 6S atmospheric and HydroLight oceanic radiative transfer models. The modeled Top-of atmosphere radiance values are evaluated using collocated observed MAN and MODIS retrievals. This study suggests that oceanic bubbles have an insignificant impact on AOD retrievals for regions with near surface wind speed less than 10 ms^{-1}. However, under high wind scenario, the impact of bubbles to aerosol retrievals is significant and needs to be considered for future AOD retrievals using passive remote sensing techniques. Lastly, one year of MODIS and Advanced Microwave Scanning Radiometer - Earth Observing System (AMSR-E) data are used to investigate the impacts of oceanic bubble to the ESOA phenomenon. This study suggests that oceanic bubbles are not the major contributor to the ESOA feature.

CHAPTER I

INTRODUCTION

Atmospheric aerosols are important atmospheric constituents and previous studies have suggested that aerosols can affect climate directly by perturbing atmospheric radiation as well as indirectly by modifying cloud physical and optical properties. In addition, the understanding of aerosols properties and their spatial and temporal distributions is critical to visibility and air quality forecasts. These applications fuel demand for accurate measurements of atmospheric aerosol properties.

Traditionally, aerosol properties are measured using three different methods: *in situ*, ground-based remote sensing, and satellite remote sensing measurements. *In situ* is a direct measurement of aerosol properties through a field experiment at a selected location. This method, while accurate, is limited in its spatial and temporal coverage. Ground-based remote sensing has an advantage over *in situ* measurements in that it allows for long-term observations at given locations. Ground based remote sensing of aerosol properties is based on measuring the attenuation of solar energy by aerosols and other atmospheric particles at specific wavelengths (sun photometry), which is then inverted to aerosol properties based on Beer's law (e.g. Holben et al., 1998). Retrievals of aerosol properties based on sun photometry are considered ground truth, and are used to validate satellite measurements. However, like *in situ* measurements, sun photometer observations are limited by their spatial coverage. Observations from space-borne satellites, in general, intercept reflected/emitted radiation from Earth's surface as well as the atmosphere with a high spatial and temporal resolution. Satellite observations have been widely

used for studying the global and regional impacts of aerosols on climate, visibility, and air pollution.

To retrieve aerosol properties from satellite measurements, a precise characterization of lower boundary conditions (e.g. surface albedo) is needed (e.g. Shi et al., 2010). Over global oceans, surface albedos are typically assumed to be a function of wind speed, with the consideration of specular and scattered reflectance as well as the reflectance due to whitecaps. Although studies have suggested that ocean bubbles could also affect ocean surface albedo (Zhang 2001, Zhang and Lewis, 2002), ocean bubbles have not been considered in the existing operational over-ocean satellite aerosol retrievals (e.g. Remer et al., 2005).

"Ocean bubbles" refer to the bubbles that are created by crashing waves. Incoming solar radiation that is reflected back into space interacts with the ocean surface in three different ways: reflected just above the surface, right at the surface, or below the surface. Radiation that penetrates the ocean surface can be reflected back by ocean bubbles formed below the sea surface. This in turn causes an increase in the amount of radiation reaching the satellite. It has been suggested from field observations that ocean bubbles evolve into a more or less horizontally uniform stratus layer of bubbles when the wind speeds are over 7 m/s. Wind speeds of this intensity can produce larger waves at a higher frequency in order to sustain the ocean bubble supply (Zhang et al., 2002). Since bubbles and whitecaps coexist, the total reflectance measured by a satellite is a sum of the reflectance from whitecaps and reflectance from bubbles. Currently, however, only the reflectance from whitecaps has been considered in the conventional satellite aerosol retrievals. Over whitecap free regions, the impacts of ocean bubbles have yet to be considered.

In the past, oceanic bubbles have been studied for the understanding of ocean optical properties including ocean surface albedo (Zhang et. al., 2002), water-leaving reflectance (Zhang 2001), and scattering of light in the ocean (Zhang et. al., 1998). Zhang (2001) discovered that the presence of an underwater bubble layer does produce an elevated yet more diffuse upward radiance field. The relationship between the enhanced background reflectance and wind speed is visible in the red and infrared because the multiple scattering is less impactful and absorption by liquid water is high such that only single-scattered photons are able to escape into the atmosphere (Zhang, 2001). Ocean bubbles have also been shown to cause a shift in the measured color of the ocean. Increased scattering causes absorption in the green spectrum to decrease, allowing more green photons to emerge from the ocean. This in turn causes the ocean color to shift from deep-blue to green (Morel et. al. 2006). This change in color can have an effect on measuring other ocean characteristics such as chlorophyll concentration. If bubbles are not accounted for, the chlorophyll concentration would be overestimated because of the color shift. This relationship increases with increasing wind speed (Zhang 2001).

This study explores the impacts of oceanic bubbles on retrieved aerosol properties. Zhang (2001) showed that whitecaps are only responsible for a fraction of the total reflectance of the ocean surface, and contributions from ocean bubbles can be significant for high wind conditions. However, in the blue and green parts of the visible spectrum, it is difficult to separate the contributions of bubbles from the total background reflectance due to the multiple scattering. In the red/infrared, water-leaving radiance is negligible and the multiple scattering is less significant, thus the bubble contributions can be determined (Zhang et al., 2002). Accordingly, in this study, the effects of oceanic bubbles on atmospheric aerosol retrievals are studied at the red/infrared channels.

One particular reason for this study is to attempt to explain the Elevated Southern Oceans Anomaly (ESOA) feature as detected by passive satellites such as MODIS and MISR. This is a band of unusually high aerosol optical depth (AOD) measurements that spans around the entire globe in the southern hemisphere around 30° S – 60° S latitude. As suggested from Figure 1, a belt of aerosol plume with high aerosol optical depth value is observed from some of the satellite products such as MODIS and MISR, but is not present in other satellite products such as the Cloud Aerosol Lidar with Orthogonal Polarization (CALIOP). Contributions from high sea salt concentrations have been suggested as one of the causes for the ESOA (Toth et al., 2013), as in the open ocean this is the primary aerosol. However, ground measurements along the southern oceans have diminished this theory to a degree. A vast portion of Maritime Aerosol Network (MAN) stations do not show elevated AOD values during high wind episodes, confirming that wind alone is not the cause of the ESOA (Toth et. al. 2013).
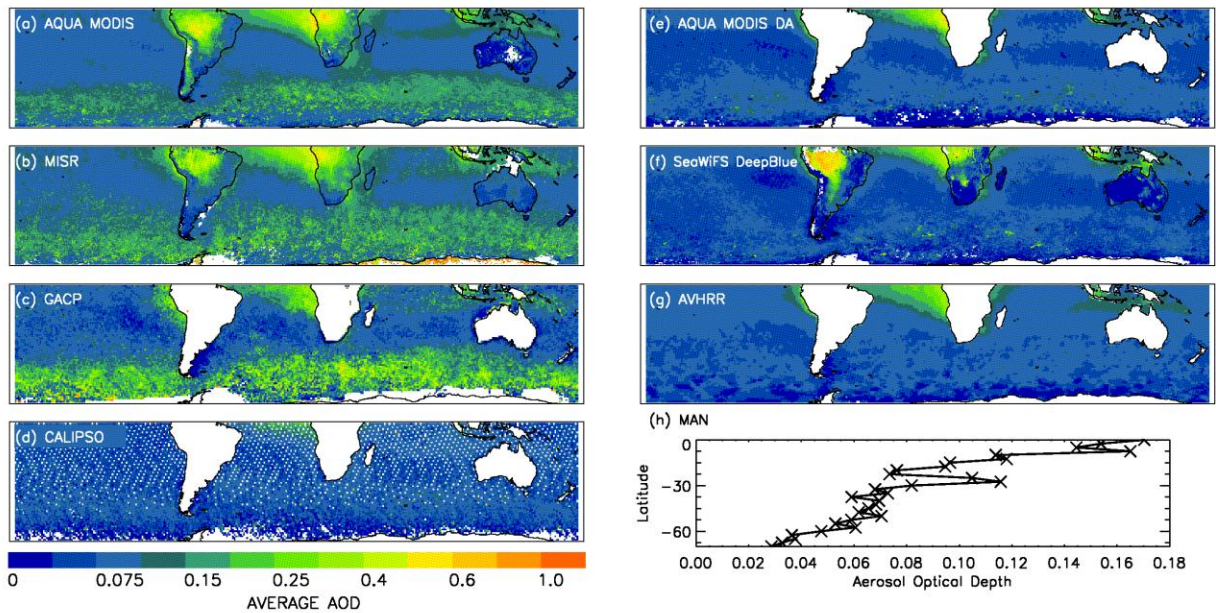
Figure 1. Courtesy of Toth et. al. (2013). This is a composition of average AOD from multiple satellites. It is clearly visible that the ESOA is not present in every sensor. Aqua MODIS and MISR show the enhanced band of AOD values, whereas CALIOP and the Sea-viewing Wide Field-of-view Sensor (Sea WiFS) Deep Blue do not.

One proven contributor is cloud contamination. Toth et al. (2013) conducted multiple experiments to show the linkage between cloud contamination and the ESOA. First, sun photometer measurements (MAN stations) were compared to the Aqua MODIS satellite measurements. It was discovered that the ESOA is not present in the MAN measurements. Therefore, further investigations were done on the MODIS data. MODIS has cloud screening capabilities, but in order to truly determine the full extent of possible cloud contamination Toth et al. (2013) utilized CALIOP, a sensor with extremely precise cloud screening methods. By collocating CALIOP and Aqua MODIS, the advanced cloud screening capabilities of CALIOP were applied to cloud-clearing of MODIS data in the ESOA region. This analysis concluded that the ESOA can be significantly reduced from cloud screening. Note that certain cloud types contributed more to the contamination than others. However the phenomenon still remains after the screening process is complete. This means that there are other contributing factors to the ESOA.

The effects of ocean bubbles on satellite radiances may be important for the understanding of discrepancies between surface- and satellite-based AOD estimates in the ESOA region. The contributions of ocean bubbles to the uncertainties in satellite retrieved aerosol optical depth are still unknown, and are studied by combining satellite observations with radiative transfer modeling. In this study, a linked oceanic and atmospheric radiative transfer model is constructed. To validate the linked radiative transfer model, the modeled TOA radiances are inter-compared with radiance observed from MODIS. Lastly, the effects of oceanic bubbles on satellite derived AOD are evaluated using the linked oceanic and atmospheric radiative transfer model for three different scenarios.

CHAPTER II

DATA AND METHODOLOGY

This study uses the Maritime Aerosol Network (MAN) data, along with satellite observations from the Moderate Resolution Imaging Spectroradiometer (MODIS) and the Advanced Microwave Scanning Radiometer - Earth (AMSR-E). The Second Simulation of a Satellite Signal in the Solar Spectrum (6S) atmospheric radiative transfer model (Vermote et al., 2006) is linked to HydroLight (Mobley and Sundman, 2012), which is an ocean radiative transfer model, for studying the effect of oceanic bubbles on aerosol retrievals. The AMSR-E data are used for providing near surface wind speed for the study. The ground-based and satellite observations, and both radiative transfer models are discussed in detail in this section.

2.1 Observational Data

The Microtops II sun photometer, which is the basic element of MAN, contains five wavelengths ranging from 0.34-1.02 μm that are used for retrieving aerosol optical depths, column ozone concentrations, and column water vapor concentrations (Smirnov et al, 2011). A GPS is used to compute position and time, and the built-in temperature and pressure sensors assist in aerosol property calculations. The measured attenuated surface radiation at the five wavelengths is used to estimate AOD based on Beer's law (Smirnov et al., 2011). Uncertainties in sun photometers come from calibration issues, changes in electronics, filter degradation, effects from the temperature, and improper pointing at the sun (waves causing the ship to sway). Even with a high number of sources for uncertainties, these errors can be minimized with the proper precautions (Porter et al., 2001, Knobelspiesse et al., 2003). In this study, MAN data are

used to validate the satellite aerosol retrievals. The reported accuracy for MAN aerosol optical depth data is ±0.02 (Smirnov et al., 2011).

The MODIS sensor is on board both the Terra (passes over the equator at 10:30 a.m. local standard time) and Aqua (equator overpass at 1:30 p.m. local standard time) platforms. MODIS, with a wide swatch of 2330 km, contains 36 spectral channels which have spatial resolutions ranging between 250 – 1000 meters. For this study, the Collection 5 MODIS Dark Target aerosol products from MODIS-Aqua (Remer et al., 2005) are used. Over the ocean, standard MODIS retrievals of aerosol optical properties are retrieved through a Look-Up Table (LUT) method in three steps. Step one: simulated satellite radiances are computed over all seven wavelengths as functions of pre-determined observing conditions and aerosol models using a radiative transfer model to form a LUT. Second, the observed satellite radiances are matched to entries in the LUT by finding the minimum difference between the satellite radiances and the LUT radiances. Finally, the aerosol parameters from the selected aerosol models and values from step 2 are used to calculate aerosol properties such as AOD. In the current over ocean retrieval algorithm, four pre-determined aerosol models are used for small mode aerosols (example, sulfate aerosols) and five are used for large mode aerosols (Remer et al., 2005). Validated against ground based observations, Remer et al. (2005) suggested that the uncertainty for the over ocean aerosol optical depth retrieval is on the order of $0.03 ± 0.05*AOD$.

Besides the MODIS Dark target aerosol products, level 1b 250 meter resolution MODIS data are collocated with wind speed data from AMSR-E and aerosol optical depth data from MAN for evaluating the radiative transfer model simulations. MODIS Channel 1 TOA radiance, along with latitude, longitude, and viewing geometry data are extracted from the level 1b

MODIS data. The MODIS cloud mask data (MOD35) are also used for excluding cloud contaminated pixels.

The near surface wind speed values are obtained from the collocated AMSR-E data. On board the Aqua satellite, the AMSR-E is a conically scanning passive microwave radiometer with 12 microwave channels (in frequency, not wavelength). Data resolution varies depending on frequency. Resolution is as low as 5 km at 89 GHz, to 56 km at 6.9 GHz. Retrieved surface parameters from AMSR-E include precipitation, sea surface temperatures, water vapor, wind speed, and other ancillary data (http://www.remss.com/missions/amsre). Since AMSR-E measures microwave radiation emitted by the surface and atmosphere, measurements are not dependent on the presence of sunlight. This is an advantage AMSR-E has over sensors that use visible channels. The data used in this study are in hourly gridded binary files with a spatial resolution of 0.25°x0.25°.

In order to find the wind speed at the MAN station, the MAN/MODIS data are collocated with the AMSR-E data in both space and time. The AMSR-E data are required to be within one hour of the MAN/MODIS data. It is important to note that multiple AMSR-E data points could match up to one MAN/MODIS point. To solve this, the spatial collocation process involves finding the closest AMSR-E point to the MAN/MODIS location. In the end, one AMSR-E data point is matched to one MAN/MODIS data point.

After collocating MODIS, MAN and AMSR-E data, the collocated data pairs that are located between 30° S and 60° S are selected for this study using four years of collocated datasets (2004, 2007, 2008, and 2009). The MODIS cloud mask data are then applied so that only confidently clear cases are inspected. After applying the regular cloud screening steps using the MODIS cloud products, all datasets are visually inspected to further exclude cloud

contaminated data points. The visual test is done using MODIS true color images. There are thirty-seven cases that pass both the MODIS cloud screening and the visual inspection. MODIS granules have been downloaded for each case for further analysis.

Next, a given MAN station needs to be located within the corresponding MODIS granule. The latitude and longitude of the station are known, making it easy to determine whether or not the station lies within the MODIS granule. The goal is to find the measured MODIS radiance at the MAN location. To do this, a box of pixels is created spanning ±0.05° latitude and longitude from the MAN station. The closest non-cloudy MODIS pixel to the MAN station is chosen. If the closest non-cloudy pixel is outside of the ±0.05° latitude and longitude box, no MODIS radiance value is assigned to that station.

2.2 Oceanic and Atmospheric Transfer Models

Both oceanic and atmospheric radiative transfer models are used in this study. To simulate TOA radiation retrieved by MODIS, the Second Simulation of a Satellite Signal in the Solar Spectrum (6S) model (Vermote et al., 2006) is used. 6S is a clear-air atmospheric radiative transfer model and has the ability to simulate TOA radiation from a vast array of satellite channels, including all MODIS channels. The equation used to calculate reflectance due to ocean bubbles is valid at the 675 nanometers spectral channel (Zhang, 2001), which lies within MODIS channel 1.

Satellite measured TOA radiation is a sum of the direct and diffuse radiation. To simulate upward TOA radiation, there are multiple components to consider: 1) Photons scattered by the atmosphere. These particles contain no information about the surface itself. 2) Photons scattered by the surface back into space. Both direct and diffuse radiation are included in this component. Direct radiation in this case is any photons scattered by the surface only. Diffuse

9

radiation is any particles that either on the way toward the surface or back into space are scattered by the atmosphere. The third and final component is where particles are scattered multiple times by the surface. Photons that are multiply scattered give inaccurate information about the surface (Vermote et al., 2006).

The ocean surface reflectance for a given viewing geometry can be assumed as a sum of four components: bubble reflectance, whitecap reflectance, specular reflectance at the ocean surface (sun glint), and scattered reflectance emerging from sea water (reflectance observed just above the sea surface). For this study, the primary focus is the contributions from bubble reflectance. Since bubble reflectance matters only over non-whitecap regions, bubble reflectance needs to be considered as a function of the whitecap coverage area. The whitecap coverage area and reflectance can be estimated based on near surface wind speed. However, the aging effects of whitecaps need also be considered. For example, Koepke (1984) summarizes it as follows: "the optical influence of whitecaps is given by the product of the area of each individual whitecap W and its corresponding reflectance $\rho_f(\lambda)$. However, the area of an individual whitecap increases with its age, while its reflectance decreases. Since whitecaps of different ages are taken into consideration in the W values, the combination of W with $\rho_f(\lambda)$ give $\rho_{wc}(\lambda)$ values that are too high". By taking this into consideration, it is not optimal to multiply the whitecap coverage area W by its individual reflectance. Instead, an effective reflectance of ocean foam patches, $\rho_{ef}(\lambda)$, and an efficiency factor, f_{ef}, are used. The effective reflectance is a constant value that is calculated based on the data input. The efficiency factor is slightly dependent on wind speed but is independent of the wavelength ($f_{ef} = 0.4 \pm 0.2$) (Koepke, 1984).

In the 6S model, the whitecap reflectance is calculated based on equations $1 - 5$. First, the whitecap coverage area is estimated based on wind speed, as shown in Eq. 1, where W is the whitecap coverage area and $wspd$ is the near surface wind speed.

$$W = (2.95 \times 10^{-6}) \times (wspd^{3.52}) \quad (Eq. 1)$$

The effective reflectance (Ref_i) from whitecaps is computed based on equations $2 - 4$, where wl is the pigment concentration, and iwl and wlp are internal parameters. For this study, pigment concentration was set constant at 20 mg/m^3.

$$iwl = 1 + int\left(\frac{wl - 0.2}{0.1}\right) \quad (Eq. 2)$$

$$wlp = 0.5 + (iwl - 1) \times 0.1 \quad (Eq. 3)$$

$$Ref_i = ref(iwl + 1) + \left(\frac{wl - wlp}{0.1}\right) \times \big(ref(iwl) - ref(iwl + 1)\big) \quad (Eq. 4)$$

Equation 5 calculates the final whitecap reflectance as the product of the whitecap coverage area W and effective reflectance Ref_i.

$$Ref_{wc} = W \times Ref_i \quad (Eq. 5)$$

Once the whitecap reflectance is calculated, the total sea surface albedo is calculated using Eq. 6 as a sum of whitecap reflectance, glint, and contributions from pigments (Vermote et al., 2006).

$$Ref_{tot} = Ref_{wc} + (1 - W) \times GLINT + (1 - Ref_{wc}) \times Ref_{wb} \quad (Eq. 6)$$

Where *GLINT* is the glint reflectance and *Ref*$_{wb}$ is the water-leaving reflectance. To account for ocean bubbles, Eq. 6 needs to be modified. To achieve this goal, 6S is coupled with the HydroLight oceanic radiative transfer model. HydroLight is designed to simulate radiative transfer processes in oceans (Mobley and Sundman, 2012), making it well-suited for estimating bubble induced surface reflectance perturbations. Select parameters in both HydroLight and 6S

models are adjusted. The parameters of interest are viewing geometry, wind speed, the ocean bubble phase function, and the ocean bubble concentration, which are used for estimating bubble reflectance.

The ocean bubble phase function is adopted from Zhang et al. (2002), where the bubble phase function is estimated from the volume scattering function (VSF). The VSF is computed from Mie scattering theory and is inter-compared with laboratory (using a volume scattering meter) and field observations. Figure 2 (from Zhang et al., 2002) shows angular scattering efficiency from both bubbles and other particles for various conditions, and at the $60° - 80°$ scattering angles bubble and particle contributions are clearly separable.
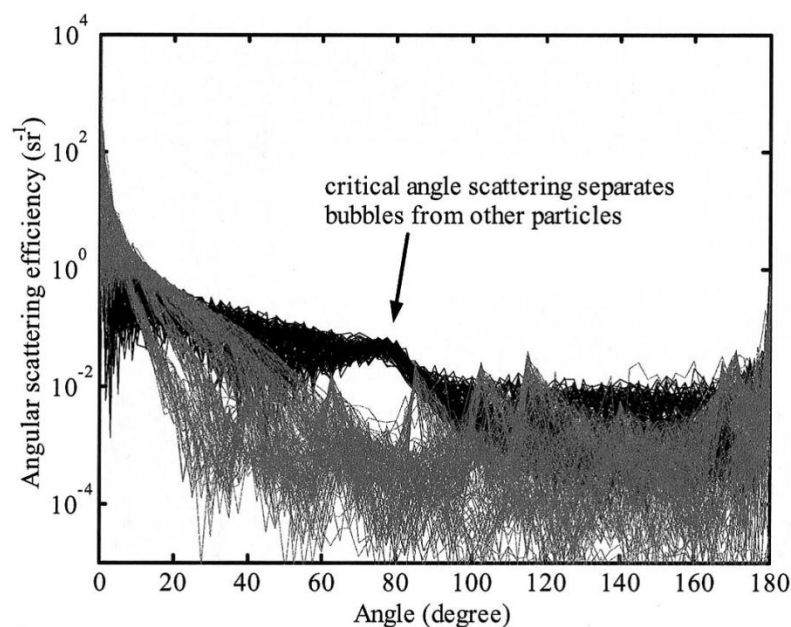
Figure 2. "The single-bubble angular scattering efficiency for bubbles (black lines) with radius between 10 and 300 μm are plotted along with the single-particle angular scattering efficiency for particles (gray lines) with refractive index of 1.02, 1.05, 1.10, 1.05, and 1.20 falling in the same size range" Zhang et al., 2002.

It is worth noting ocean bubbles inevitably get covered in some sort of organic coating of varying thickness. Including the coating in optical computation is critical for remote sensing applications because it can increase backscattered light by ocean bubbles by a factor of up to 4

(Zhang et al., 1998). Little is known about the composition and thickness of bubble coatings. However a recent study shows that a coating of proteinaceous type (D'Arrigo 1983; D'Arrigo et al., 1984) with a refractive index of 1.18 relative to water and a thickness of 0.01 μm provides the best match between optical and acoustical observations of bubbles (Czerski et al, 2011). In simulations, the bubble phase function is assumed to remain constant regardless of wind speed and in this study the organic coating is represented within the phase function.

Bubbles in the upper ocean are primarily generated by breaking ocean waves (Thorpe and Humphries, 1980; Lamarre and Melville, 1991). When wind speeds exceed 7 m/s, field observations have shown that a stratus layer of bubbles form under the sea surface and persist as a result of a continuous supply of bubbles from frequent wave breaking and subsequent advection by turbulence (Thorpe 1982; Thorpe 1986; Crawford and Farmer 1987). Because of the rapid rising of bubbles, the density distribution of the ocean bubbles decreases exponentially with depth while overall concentrations increase with increasing wind speeds following a power law. Ocean bubble concentrations in this experiment are obtained from (Zhang 2001; Zhang and Lewis, 2002), in which the concentrations at different layers are modeled as a function of wind speeds based on field observations.

2.3 Estimating Bubble Surface Reflectance

HydroLight is a Windows-based program. For this study, the Windows-based HydroLight program is inverted to a Linux-based version to speed up the processes. The outputs from the Linux and the Windows versions of HydroLight are inter-compared to ensure the conversation does not introduce errors into the calculations.

To study the contributions of bubbles to aerosol retrievals, the effects of bubbles on the surface reflectance need to be known. The contribution from ocean bubbles adds to the surface

reflectance used in the aerosol retrieval. Background reflectance is easily found by running HydroLight with the bubble concentration set to zero. To get the contribution from ocean bubbles, the difference is taken between HydroLight runs with a bubble concentration of zero and one with a concentration greater than zero. To get an equation that represents the bubble concentration, this reflectance difference is plotted against wavelength. The results are shown in Fig. 3. These results are a recreation of a plot from Zhang (2001). The default bubble concentrations are obtained from Zhang (2001). The phase function is based on Zhang et al. (2002), which used controlled laboratory conditions to get an accurate phase function from the volume scattering function.
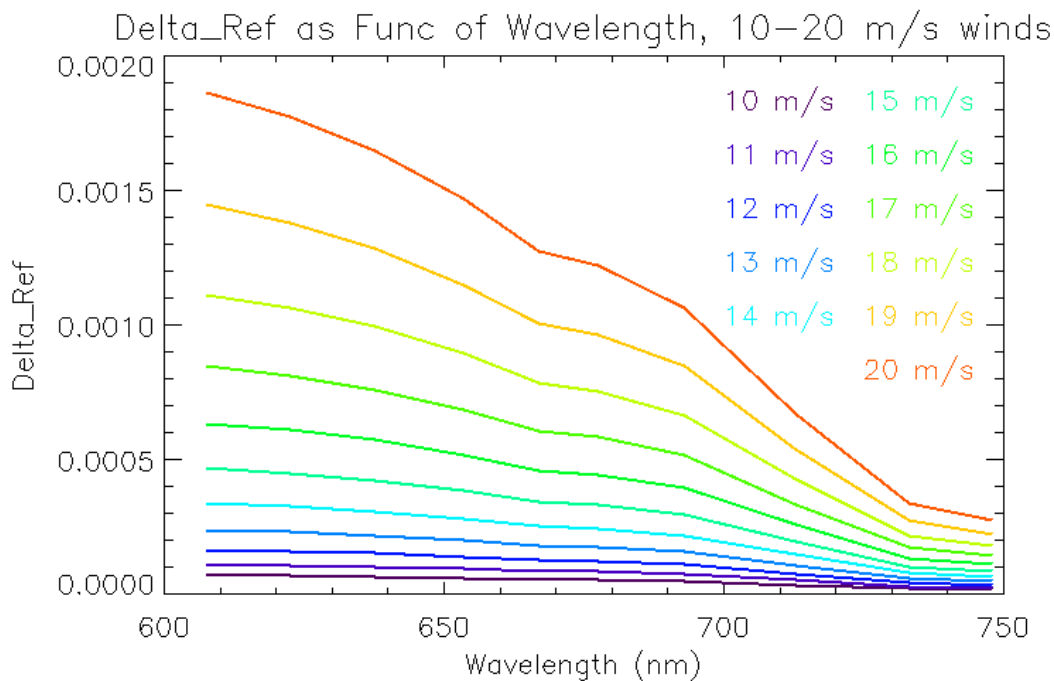
Figure 3. This is the reflectance difference between the default bubble concentration and a bubble concentration of zero. It is plotted as a function of wavelength. The equation is valid at 675 nm, so that is the wavelength in which a linear fit will be done to come up with an equation that can calculate the contribution from ocean bubbles at the given concentration.

Note that multiple scattering is significant in the lower wavelengths of the visible spectrum (e.g. green and blue channels). Therefore, the ocean bubble contributions cannot be

14

discerned from the overall background reflectance. Multiple scattering is far less in the red/infrared spectral channels, making it much easier to separate the ocean bubble reflectance from the background. It is for this reason that 675 nanometers is the chosen wavelength.

According to Zhang (2001), the format of the equation used to calculate bubble contribution is as shown in Eq. 7, where L and J are the desired coefficients.

$$\Delta Ref_{bub} = L \times wspd^J \quad (Eq.7)$$

Instead of applying an exponential fit, taking the natural log of Eq. 7 will result in a linear equation (y = ax + b) that can be used to easier determine the coefficients L and J.

$$\ln(Ref_{bub}) = \ln(L) + J \times \ln(wspd) \quad (Eq.8)$$

Equation 9 represents the change in reflectance caused by ocean bubbles based on the work done by Zhang (2001). To properly modify 6S, Eq. 9 is first modified and then added to Eq. 6. The resulting equation is Eq. 12 shown in the next chapter.

$$\Delta Ref_{bub} = \pi \times \left((4.82 \times 10^{-9})(wspd^{4.55}) + (1.08 \times 10^{-6})(wspd^{2.55})\right) \quad (Eq.9)$$

For further testing, an experiment is done using upper and lower boundaries of the bubble concentrations. The upper boundary is made by doubling the default bubble concentrations, while the lower boundary is represented by half of the default concentrations. The use of upper and lower boundaries allows analysis of two extreme conditions when compared to a normal set of conditions.

CHAPTER III

RESULTS AND DISCUSSION

3.1 Update the 6S Model to Account for Ocean Bubbles

The original equation to account for ocean bubbles is represented by Eq. 9. This equation is valid at 675 nanometers. The first term represents the contribution from ocean bubbles while the second term is the contribution from whitecaps. Figure 4 depicts the whitecap reflectance as a function of wind speed from Koepke (1984). The expected result is that the reflectance and also the difference in the reflectance (comparing bubbles being present and not present) both increase exponentially with increasing wind speed. However, preliminary results did not correspond with the expectations. One possible reason for this is sun glint.
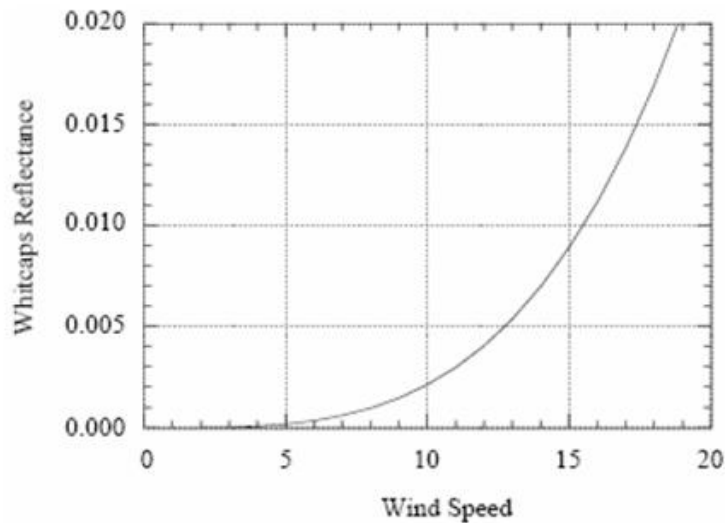

Figure 4. Whitecap reflectance plotted as a function of wind speed according to Koepke (1984). There is an exponential increase in reflectance due to whitecaps with increasing wind speed.

When the solar zenith angle (SZA) and viewing zenith angle (VZA) are similar in value, but are located nearly 180 degrees opposite to each other at the azimuth plane (or near zero glint angle), strong specular reflection is expected (sun glint contamination). Within the glint regions, specular reflectance of solar radiation dominates the TOA radiation received by the satellite and surface contributions from whitecaps and bubbles become negligible. Away from the sun glint angular domain, the expected results from Fig. 4 are observed. Figure 5 is an example of 6S simulated reflectance (at 675 nm) plotted against wind speed at four different glint angles. Here the cloud and aerosol free standard atmospheric profile is used with the solar zenith angle (SZA) set to 0 degrees and the viewing zenith angle (VZA) is varied from 0 to 60 degrees. By varying the VZA, the glint angle varies from 0 to 60 degrees. The glint angle is calculated using Eq. 10.

$$glinta = \cos^{-1}(\cos(sza)$$

$$\times \cos(vza) - \sin(sza) \times \sin(vza) \times \cos(sazm - vazm)) \times \frac{180.0}{\pi} \quad (Eq.\,10)$$
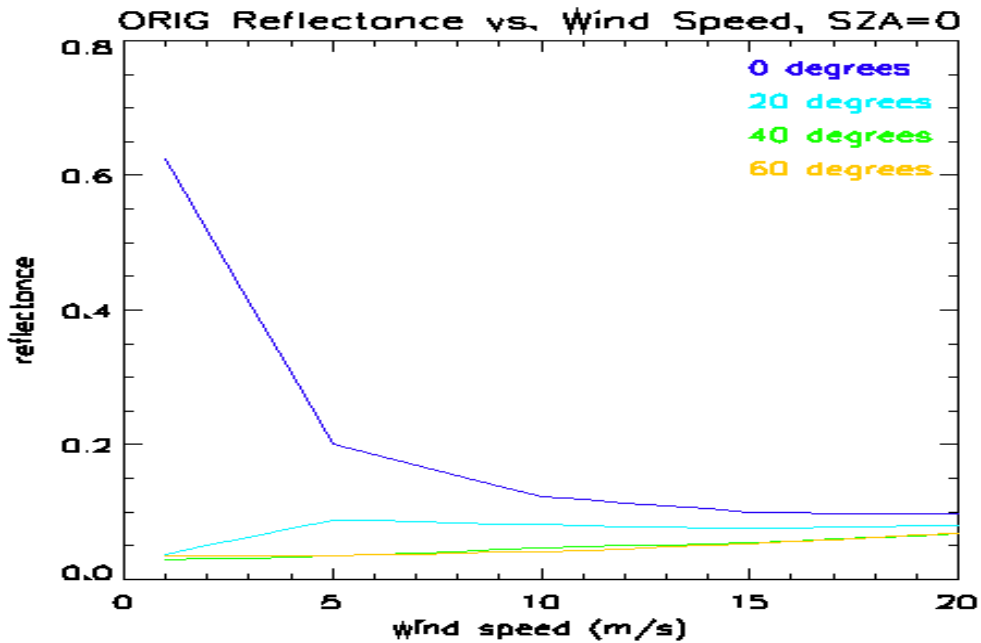

Figure 5. 6S reflectance plotted as a function of wind speed (m/s). The solar zenith angle is constant at 0°. Sun glint is still present at lower glint angles. However the exponential growth in reflectance begins to show up at higher glint angles.

Note that Eq. 9 is from Zhang (2001). It includes contributions from both bubbles and whitecaps. However, the surface reflectance pattern from whitecaps as represented in Eq. 9 is found to be inconsistent with the whitecap reflectance calculations from 6S (Eq. 5). To best preserve whitecap reflectance calculations, Eq. 5 is best suited for this study. Therefore only the bubble portion of Eq. 9 is utilized in this study. Equation 11 is then multiplied by (1-W) and added to the end of Eq. 6 to properly take into account ocean bubbles in the 6S radiative transfer model.

$$\Delta Ref_{bub} = \pi \times \left((4.82 \times 10^{-9})(wspd^{4.55}) \right) \quad (Eq.11)$$

$$Ref_{tot} = Ref_{wc} + (1 - W) \times GLINT + (1 - Ref_{wc}) \times Ref_{wb} + (1 - W) \times \Delta Ref_{bub} \quad (Eq.12)$$

Clearly a difference is expected in the 6S simulation when Eq. 6 is replaced with Eq. 12 to give a more complete consideration of ocean bubbles. A preliminary test is conducted with results shown in Fig. 6. The differences in simulated reflectance at 675 nm with and without inclusion of oceanic bubbles are plotted against wind speed for four viewing zenith angles (0, 20, 40, and 60 degrees). A cloud and aerosol free standard atmospheric profile is used and the solar zenith angle is constant at 0 degrees. Results in Fig. 6 show the expected relationship between the change in reflectance between the scenarios with and without the consideration of oceanic bubbles as a function of near-surface wind speed. This proves that the new equation inserted into 6S is functioning.
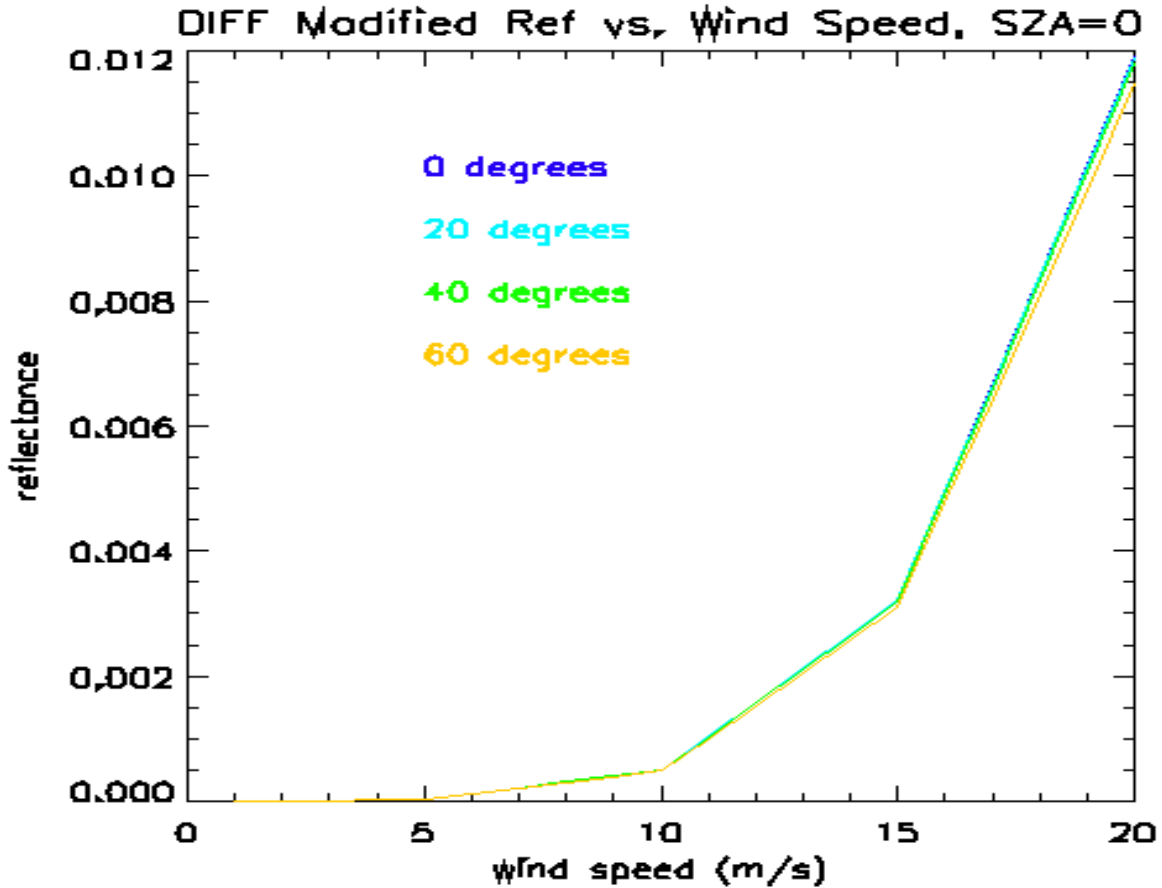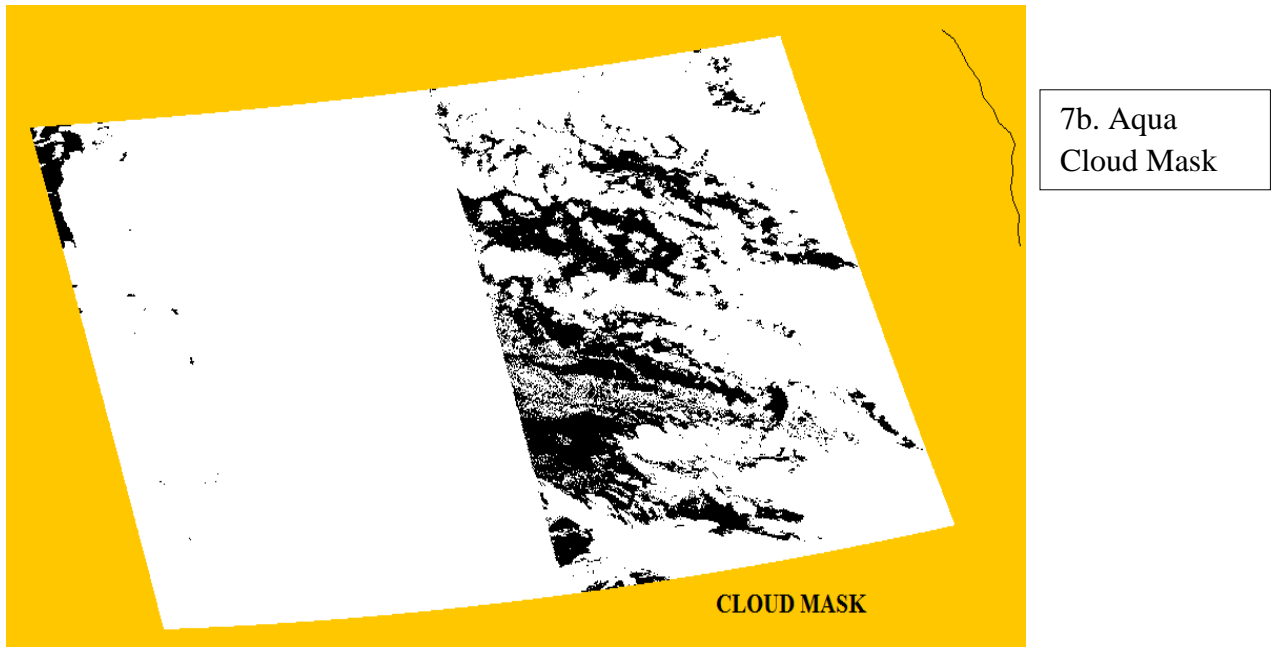
Figure 6. Difference in 6S reflectance between bubble and no bubble cases as a function of near-surface wind speed for varying viewing zenith angles.

3.2 Evaluate the Original 6S Model

The next step involves comparison of the original 6S simulated MODIS radiance with the observed MODIS radiance data at 675 nm. The analysis of the 6S model calculations after adding ocean bubble contributions is discussed later. MAN, Aqua MODIS, and AMSR-E data are collocated in order to construct an observation-based group of data that includes AOD from MAN, wind speed from AMSR-E, and satellite radiance from MODIS. The MODIS cloud mask data are used to eliminate all cloud contamination scenes. The cloud-clearing step is needed to create a clear-air condition. Shown in Fig. 7, a small scale test is performed on an Aqua MODIS image to ensure that the MODIS cloud mask data are applied correctly. Figure 7a shows the

Aqua MODIS radiance for November 21, 2009 from the MODIS Dark Target products. Figure 7b shows the results of the MODIS cloud masking data and Fig. 7c shows the Aqua MODIS radiance field after the cloud masking process. Only confidently clear pixels are chosen in hopes of eliminating any possible cloud contamination.

7a. Aqua Radiance Data

MODIS RADIANCE

0.0   3.0   6.0   9.0   12.   15.   18.   21.   24.   27.   30.

7b. Aqua Cloud Mask

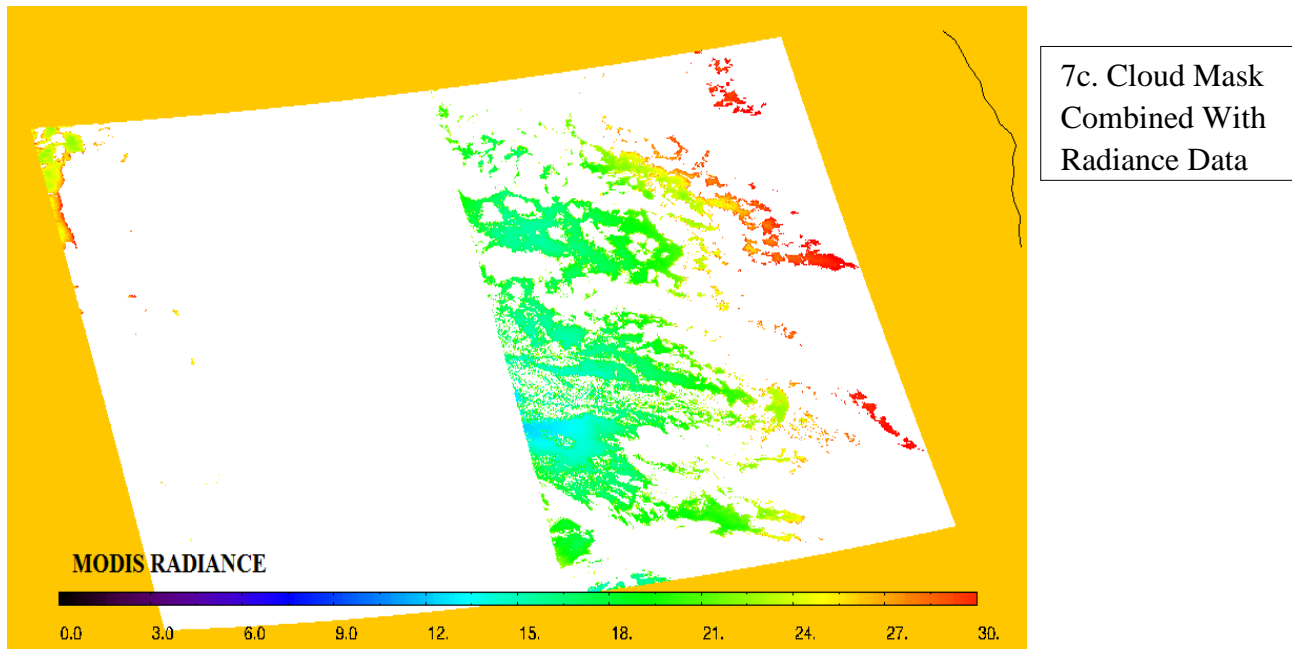**CLOUD MASK**

7c. Cloud Mask Combined With Radiance Data
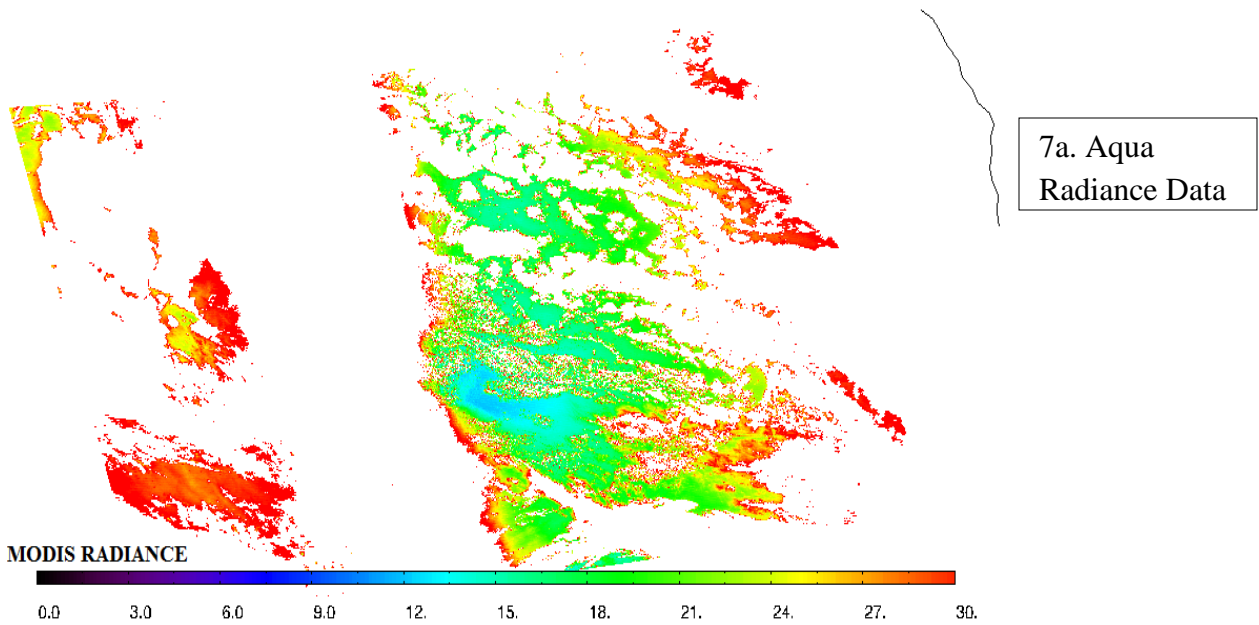
Figure 7. a) Aqua MODIS radiance data. Areas of white indicate likely cloud or glint. b) Aqua MODIS cloud mask product for the same granule as 7a. The black is confidently clear data and white is any pixel flagged as cloud. c) Combination of the top and middle to evaluate the performance of the cloud mask product.

The closest MODIS cloud free pixel to a given MAN station is used to represent the MODIS reflectance value. Figure 8 shows the comparisons between MODIS observed radiance at 650 nm and 6S simulated MODIS spectral channel 1 radiance for all four years of data using the unmodified 6S model. To simulate the observed radiance, AOD from MAN, wind speed from AMSR-E, and viewing geometry from MODIS are used as the input parameters for the 6S simulations. The default oceanic aerosol model from 6S (Vermote et al., 2006) is also selected for the simulation to account for background ocean aerosol characteristics.
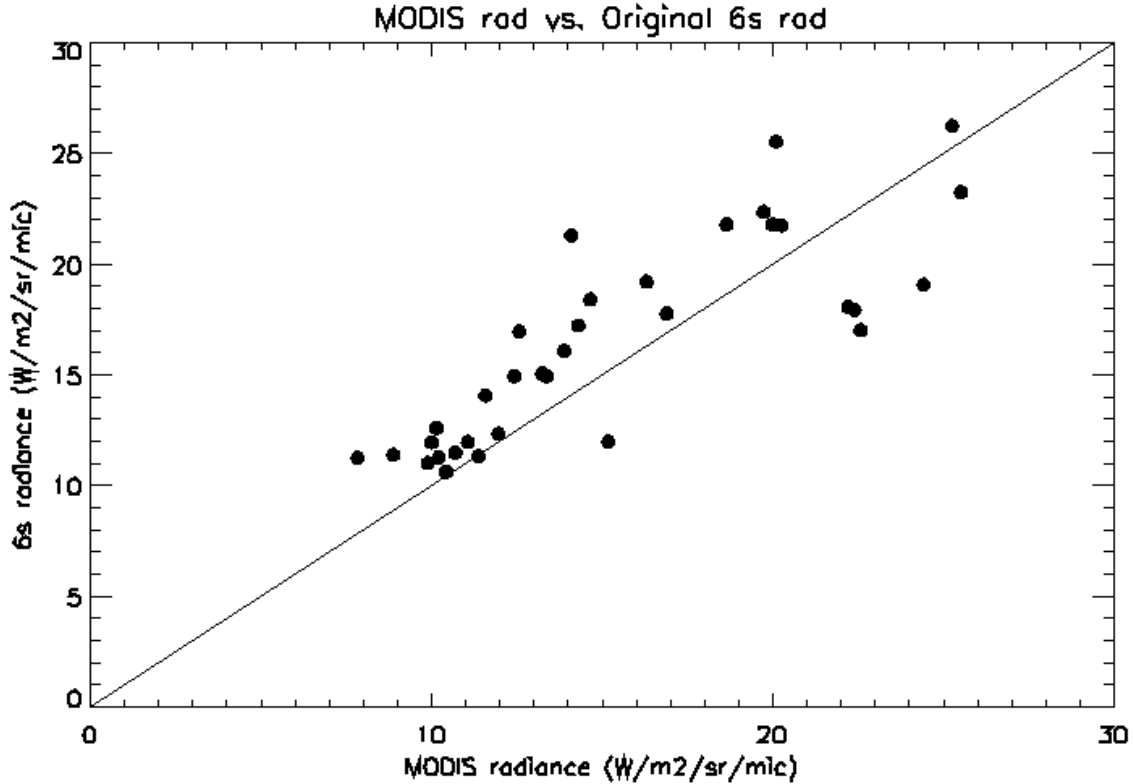
Figure 8. 6S simulated radiance ($Wm^{-2}sr^{-1}\mu m^{-1}$) and MODIS observed radiance ($Wm^{-2}sr^{-1}\mu m^{-1}$) for all years of data.

Biases in the simulated radiance values can be clearly seen that may relate to uncertainties in measured properties including wind speed and AOD. Also, the default ocean surface reflectance pattern, the oceanic aerosol model, and the standard atmospheric profile assumed in the model runs could also contribute to the biases in the simulations. Still, Figure 8 suggests that 6S can be used to simulate MODIS radiance with reasonable accuracy.

3.3 Bubble Impact Study Using the Collocated MODIS and MAN Data

After validation of the 6S model against observations, we attempt to determine the impacts of oceanic bubbles on the retrieved aerosol optical depth using the collocated MODIS and MAN datasets. Sensitivity studies are first performed to evaluate the changes in TOA radiance in response to changes in AOD as a function of wind speed using the collocated data

from November 29, 2004. For this case the SZA is 44.02° and the VZA is 11.25° as retrieved

from MODIS. Figure 9 shows the 6S modeled TOA reflectance from MODIS channel 1 as a

function of AOD and wind speed without considering ocean bubbles. The wind speed is varied

from 1.0 to 20.0 m/s and AOD from 0.01 to 0.20. It is seen in Fig. 9 that at lower wind speeds

(e.g. < 7 ms^{-1}) the reflectance values do not change drastically at the given range of AOD values.

When the wind speed becomes greater than 15 ms^{-1}, the change in reflectance is much more
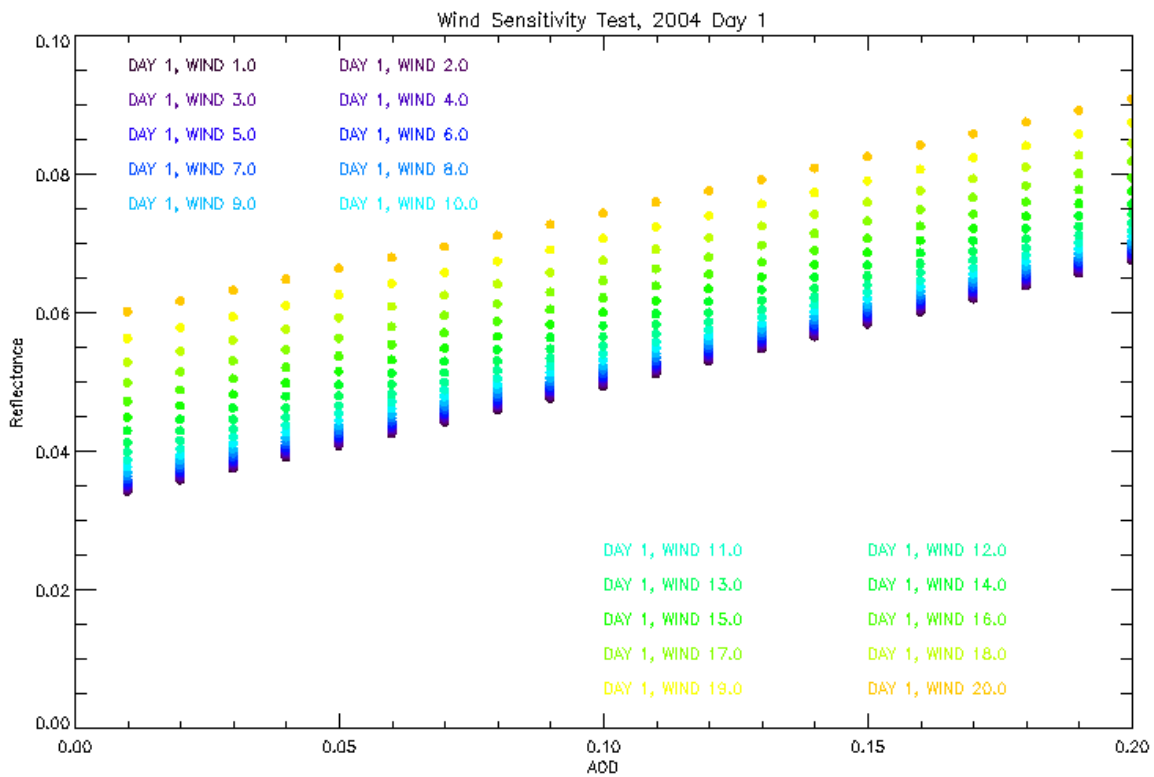
significant.

Figure 9. 6S modeled TOA reflectance from MODIS channel 1 as a function of AOD and wind
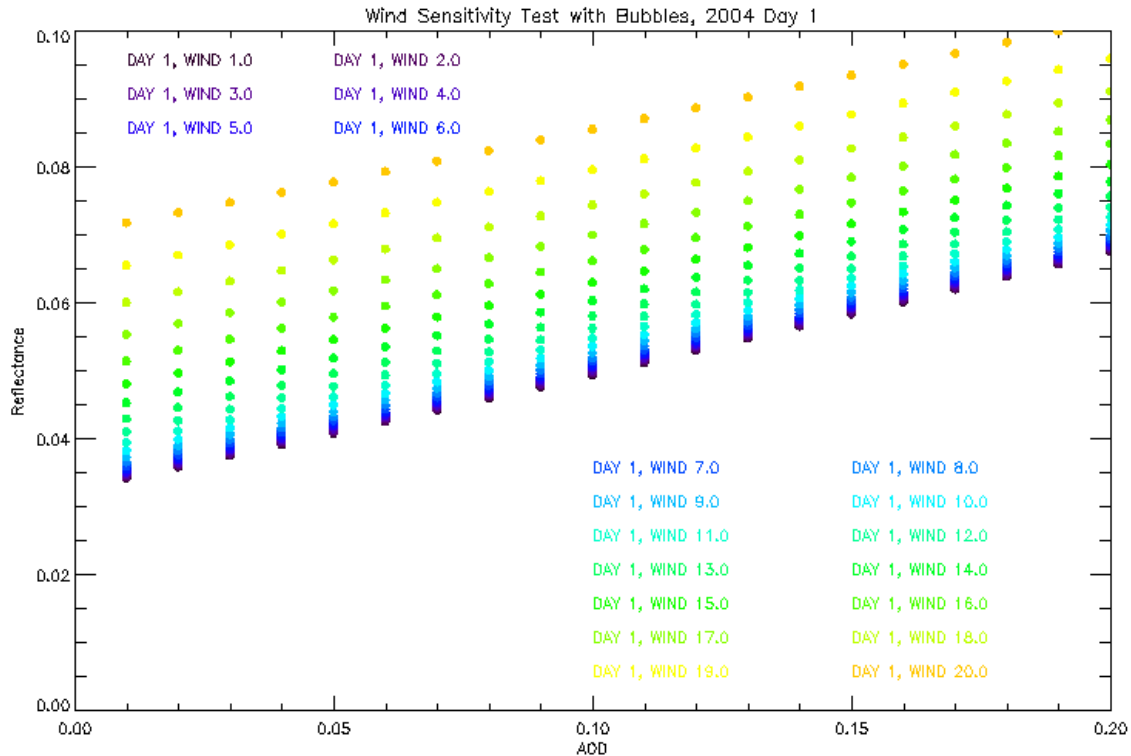speed without considering ocean bubbles (data from November 29, 2004).

Figure 10. Data from Fig. 9 with the inclusion of ocean bubbles.

Figure 10 shows the same information as Fig. 9 except with the inclusion of ocean bubbles. Comparing Fig. 10 with Fig. 9, there is a significant increase in the reflectance values, in particular at higher wind speeds. Not only do the reflectance values increase at higher wind speeds, the changes in reflectance with increasing wind speed also increase. At lower wind speeds the changes in reflectance are still relatively small.

Next, the impact of bubbles on AOD retrievals are studied using the 37 observations mentioned in chapter 2. These include AOD (MAN), wind speed (AMSR-E), and channel 1 MODIS radiance. However, attempts to ascertain the effects of ocean bubbles are not successful as the impacts of oceanic bubbles on MODIS radiance are comparable in magnitude to the uncertainties in the modeled MODIS radiance values as shown in Figure 8. Also, standard atmospheric model profiles are used which may differ from the atmospheric profiles of the observed scenes. Other methods are needed to study the impacts of bubbles to AOD retrievals.

24

3.4 Theoretical Analysis of Bubble Impacts

Since an observational based analysis yields inconclusive results, a theoretical approach is applied next to investigate bubble impacts. Look-Up-Tables (LUT's) of simulated MODIS TOA reflectances are constructed as function of solar zenith angle and viewing zenith angle (each varies from 0° to 60° at intervals of 10°), solar and viewing azimuth angle (from 0° to 180° at intervals of 30°), AOD (from 0.01 to 0.4 at intervals of 0.01), and wind speed (varies from 1.0 m/s to 20 m/s). The LUTs are constructed for two scenarios: one with the inclusion of ocean bubbles and one without. The modified 6S model is used in the simulation. Here simulations of most observational conditions are attempted and average impacts of ocean bubbles on AOD retrievals are derived.

For the purpose of this sensitivity study, two additional scenarios are also included: "double bubble" and "half bubble". "Double" indicates that the bubble concentration is two times that of the default values, and "half" represents a bubble concentration that is only one half of the default value. This is done to examine the effects of bubble concentration on AOD. Varying the bubble concentration is done to create an uncertainty envelope. The 6S model needs to be modified to account for both the "double bubble" and the "half bubble" cases. Equation 9 is derived by Zhang (2001) and cannot be used because it will not properly compare to the equations derived in this experiment for "double" and "half" bubble concentrations. Therefore the same method as Zhang (2001) is adopted to create three new equations. Using HydroLight, the reflectance difference between runs with each bubble concentration and runs with zero bubble contribution are plotted against the wavelength. A linear fit was done at 675 nanometers because it is at this wavelength that whitecap reflectance does not dominate over ocean bubbles which allows the contribution of ocean bubbles to be extracted accurately. The derived

equations are shown below where equations 13, 14, and 15 are for Default Bubble, Double

Bubble, and Half Bubble cases respectively.

$$\Delta Ref_{bub} = \pi \times \left((1.60 \times 10^{-9})\left(wspd^{4.52}\right)\right) \quad (Eq.\,13)$$

$$\Delta Ref_{dbl} = \pi \times \left((2.50 \times 10^{-9})(wspd^{4.62})\right) \quad (Eq.\,14)$$

$$\Delta Ref_{half} = \pi \times \left((8.97 \times 10^{-10})(wspd^{4.47})\right) \quad (Eq.\,15)$$
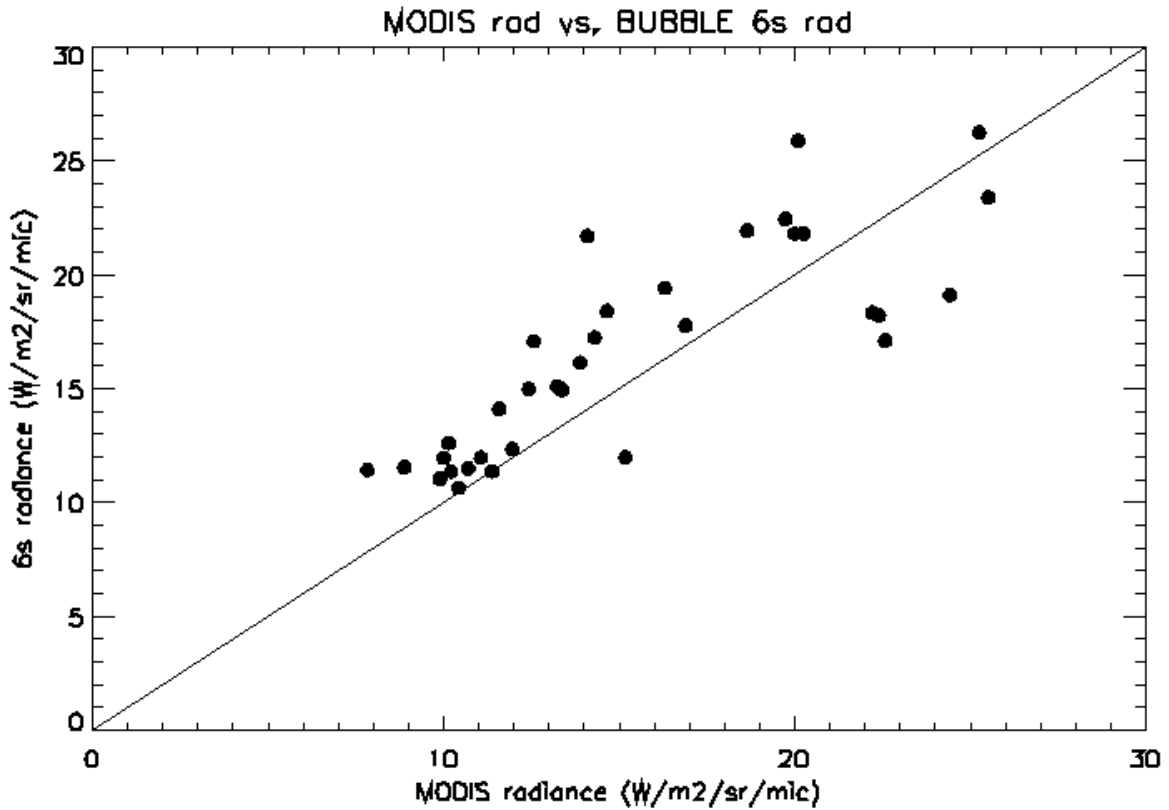
Figure 11. This is a composition of 6S radiance (Wm^{-2}sr^{-1}μm^{-1}) plotted against Aqua MODIS radiance (Wm^{-2}sr^{-1}μm^{-1}) for the default bubble concentration.

To further validate these equations, each is individually inputted into Eq. 12 and

experiments similar to those in section 3.2 are conducted for simulating radiance values and

inter-comparing with the observed MODIS radiance values (see Fig. 8). Figure 11 shows the

comparisons between the 6S simulated radiance values and the MODIS observed radiance for

the default bubble cases. Similar results are found for both the half and double bubble cases and thus are not shown. All three cases compare reasonably with the observed radiance, although the effects of ocean bubbles are not readily visible. Clearly, testing the effects of bubbles on aerosol retrievals may not be sufficient with a small collection of data pairs as shown in section 3.3. A large scale generalized test is necessary for investigating the averaged effects of oceanic bubbles on aerosol retrievals as well as the threshold conditions at which ocean bubbles become a significant factor in satellite aerosol measurements.

For any given observing conditions, the simulated reflectances (for both with and without bubble cases) are used to compute the errors in the retrieved AOD without considering bubbles. For example, for a given bubble case with a given wind speed and fixed viewing geometry, a relationship between AOD (AOD_{bub}) and simulated TOA reflectance is established. For the same observing conditions, the simulated reflectance is then used to search for the corresponding AOD value for bubble free conditions (AOD_{no_bub}). The difference between AOD_{bub} and AOD_{no_bub} (ΔAOD) represents the simulated retrieval error without considering ocean bubbles in the retrieval process. Note that the process is done for default, double, and half bubble concentration cases.

Select results are presented to examine the importance of bubble effects as a function of viewing geometry as well as bubble concentration. A single day is chosen from the list of 37 cases mentioned in chapter 2, January 12, 2008. Results are found for solar zenith angles (SZA) of 0°, 30°, and 60°.

3.4.1   Fixed SZA, SAZM, VAZM and AOD_{bub}

Figure 12 is a plot of change in AOD against wind speed. The SZA is 30° while the solar azimuth angle of 0°. The change in AOD (ΔAOD) is found using a starting

AOD value (AOD$_{bub}$) of 0.1. Colors are used to identify each bubble concentration while shapes are associated with different viewing zenith angles (VZA). At all lower wind speeds the changes in AOD are minor regardless of the bubble concentration. As wind speed increases, there is an exponential increase in ΔAOD, with a much more significant ΔAOD at wind speeds greater than 10 m/s.
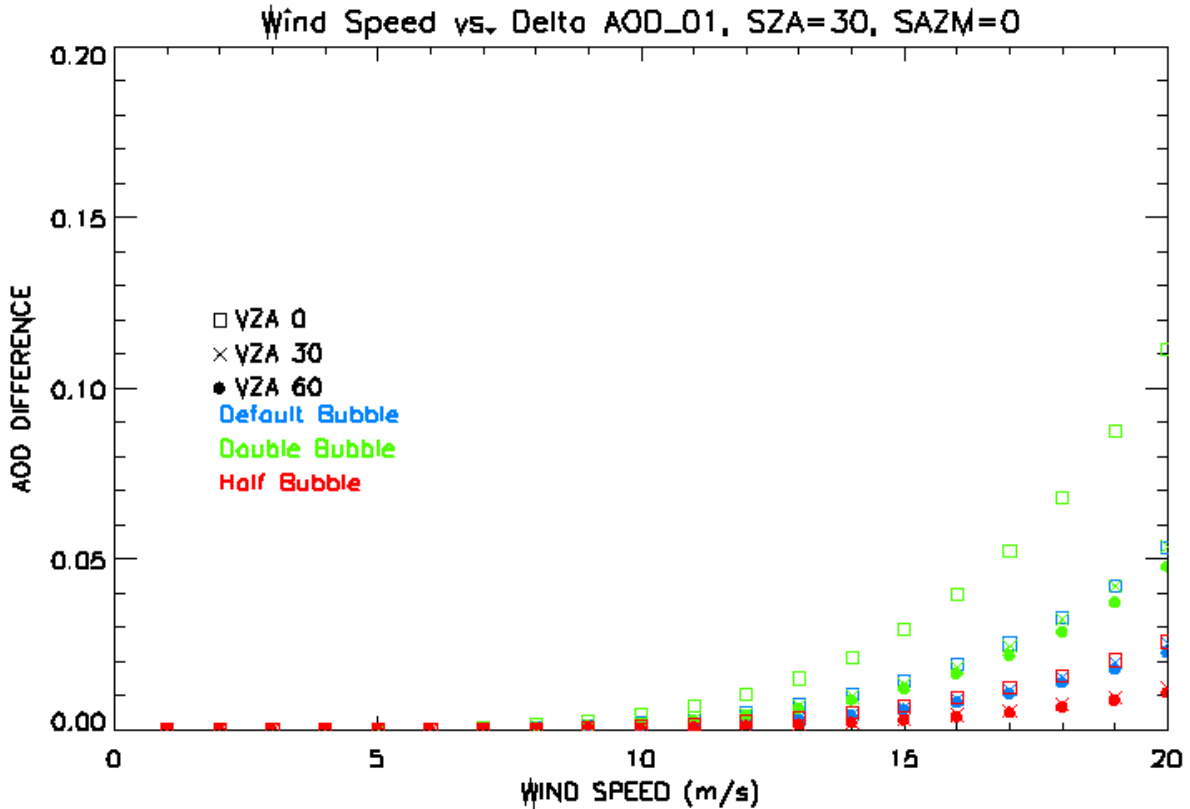

Figure 12. This is the change in AOD using a starting AOD value of 0.1 at a solar zenith angle of 30° and a solar azimuth angle of 0°.

The AOD difference is also dependent on the bubble concentration. This is seen when comparing the three concentrations at one viewing zenith angle. For any viewing zenith angle in Fig. 12, the half bubble concentration has the lowest change in AOD while double bubble has the highest AOD difference. It is expected that changing the bubble concentration will have an effect on ΔAOD, but it is uncertain how significant the

effect is. It is apparent that at higher wind speeds the bubble concentration becomes an important variable.

3.4.2 Fixed SZA, SAZM, VAZM, and variable AOD$_{bub}$

The change in AOD as a function of wind speed, VAZM, and bubble concentration for three different AOD$_{bub}$ values is examined. Figures 13 and 14 show the change in AOD using starting AOD values of 0.2 and 0.3 respectively with the same viewing geometry as Fig. 12. Changing AOD$_{bub}$ does not appear to have an effect on ΔAOD based on the results in Fig. 13 and Fig. 14.
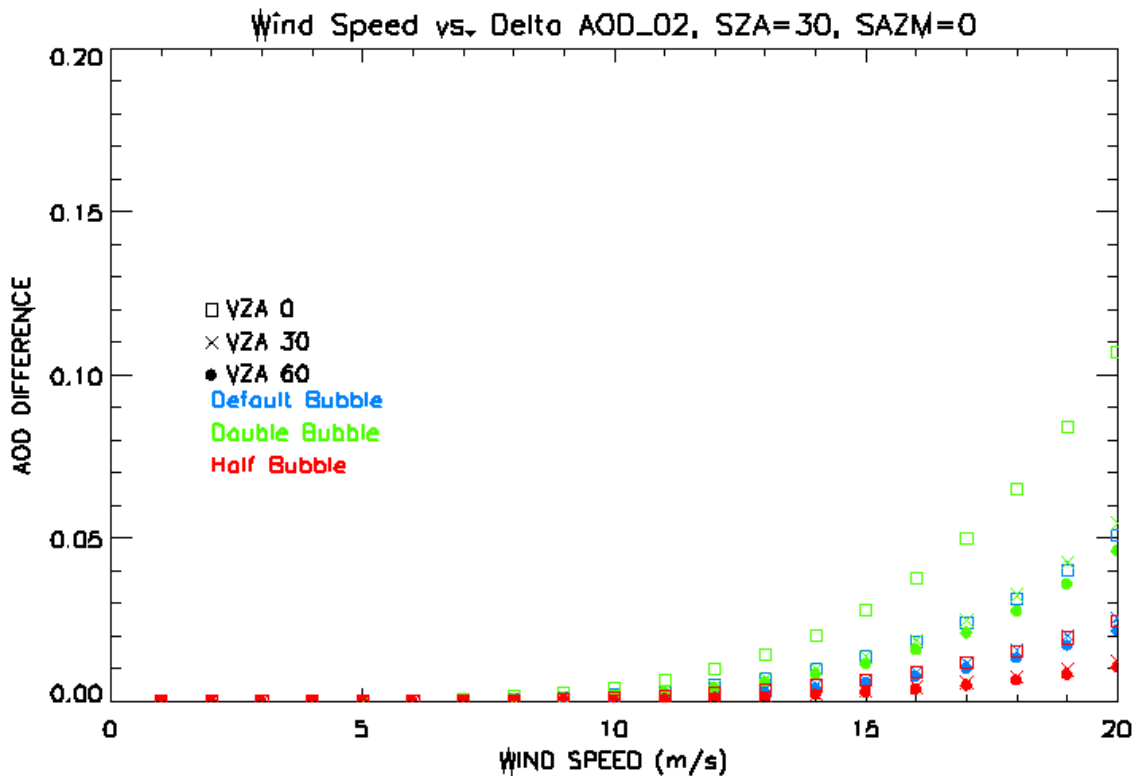

Figure 13. ΔAOD plotted against wind speed with a solar zenith angle of 30, solar azimuth angle of 0, and the starting AOD value was 0.2.
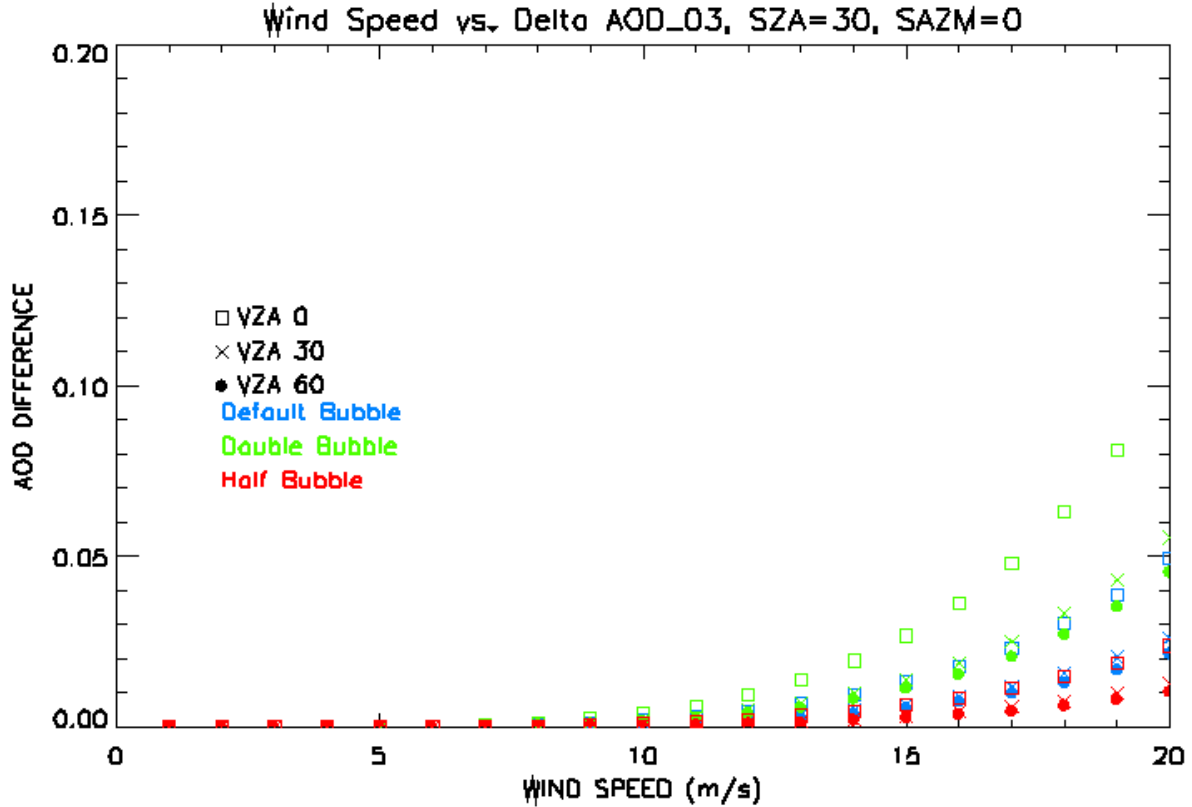
Figure 14. ΔAOD plotted against wind speed using a starting AOD value of 0.3.

3.4.3 Fixed SZA, varied AOD$_{bub}$, averaged

To remove the consideration of the viewing geometry, ΔAOD values are averaged at a constant SZA for all VZAs and SAZMs. Averaging is performed for each AOD$_{bub}$ (0.1, 0.2, and 0.3). This makes it easier to compare the effects of varying bubble concentrations on AOD. Also glint angle (Eq. 10) is calculated for all viewing geometry combinations. To eliminate any possibility of sun glint contamination, data are averaged only if the glint angle is greater than 30 degrees. Figure 15 shows the average ΔAOD plotted against wind speed for each starting AOD value for a solar zenith angle of 30°. Similar to Figures 12-14, the effect of ocean bubbles is significant only for cases with near surface wind speeds over 12 m/s. Double or half the default bubble concentration

can have a significant effect to aerosol retrievals as well, but again, only for wind speeds greater than 12 m/s.
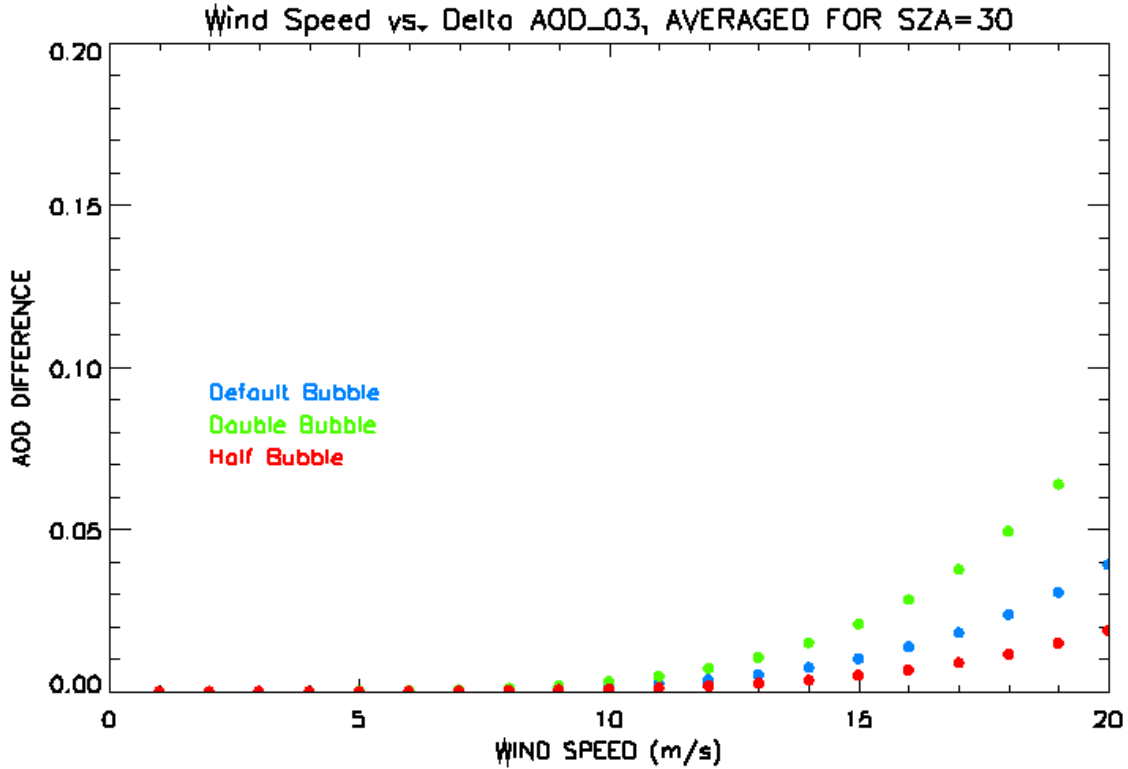

Wind Speed vs. Delta AOD_01, AVERAGED FOR SZA=30

Wind Speed vs. Delta AOD_02, AVERAGED FOR SZA=30
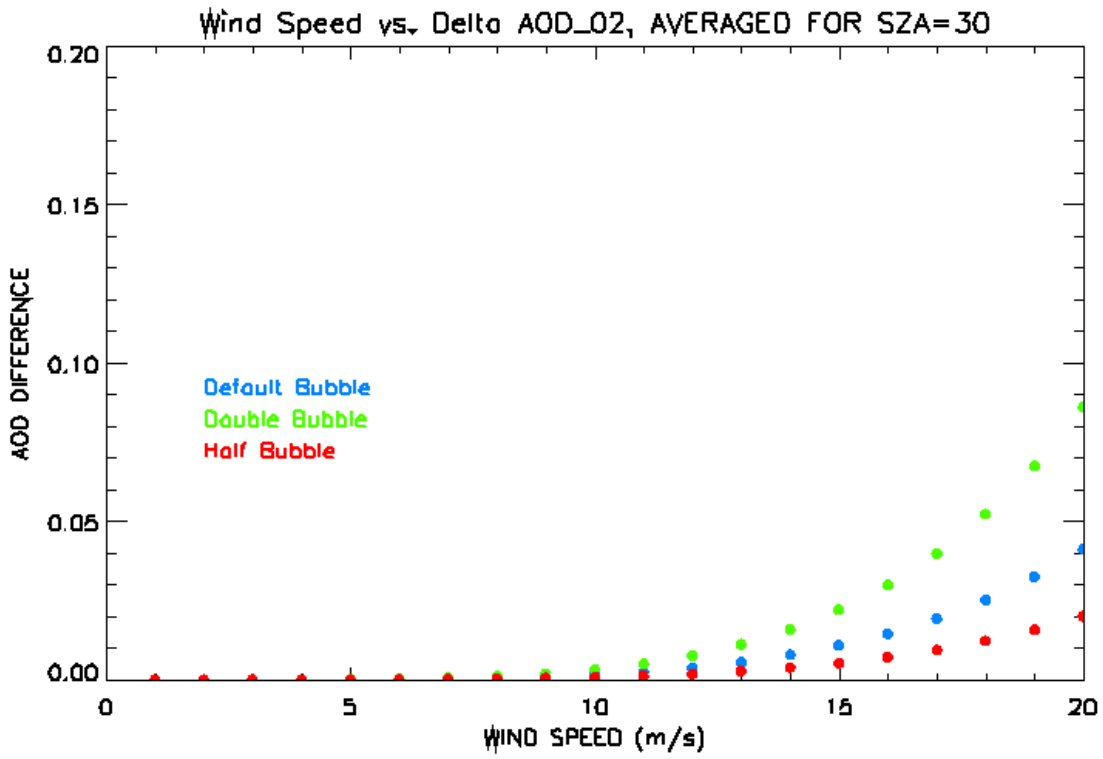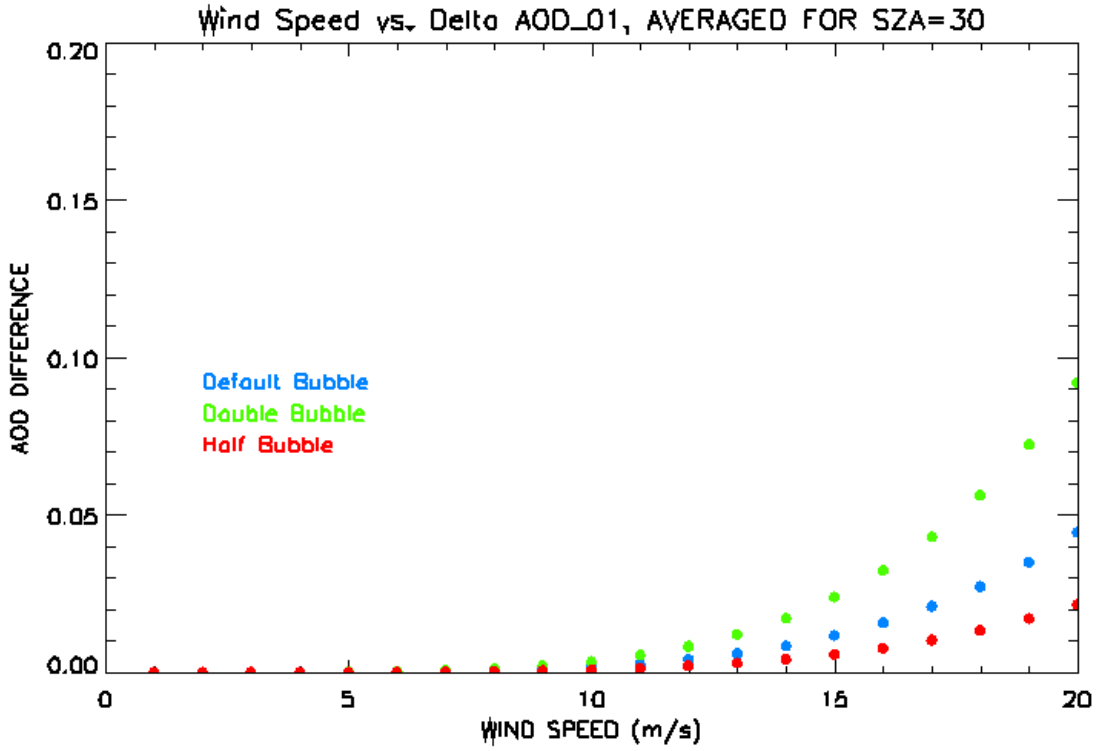
Figure 15. Averaged ΔAOD plotted as a function of wind speed for SZA of 30° at top) AODbub=0.1, middle) 0.2, and bottom) 0.3. Viewing geometry is eliminated as a variable, allowing strictly analysis of the bubble concentrations.

Sun glint contamination causes uncharacteristically high ΔAOD values. The reasoning behind this is illuminated in Fig. 16, where reflectance is plotted against AOD at a constant wind speed. There are times when the change in reflectance between "no bubbles" and "bubbles" is very small. Figure 16 is an example of one of these cases that also contains a shallow slope. In order to illustrate the actual variations in reflectance, the y-axis is restricted to range from 0.1 to 0.12. Observed from Fig. 16, at an AOD value of 0.3, the reflectance value for "with bubbles" is 0.109283. At AOD values greater than 0.3, the reflectance values for "no bubbles" do not reach this value. In fact the only spot in which "no bubbles" does reach this value is between 0.05 and 0.06 AOD. This makes for a ΔAOD of around 0.25. Other cases have situations where one or more

starting AOD values have multiple ΔAOD results. This happens when the parabolic shape seen in Fig. 16 has repeated reflectance values. When sun glint is taken into account, all uncharacteristically high ΔAOD results are eliminated and therefore do not appear in Fig. 15.
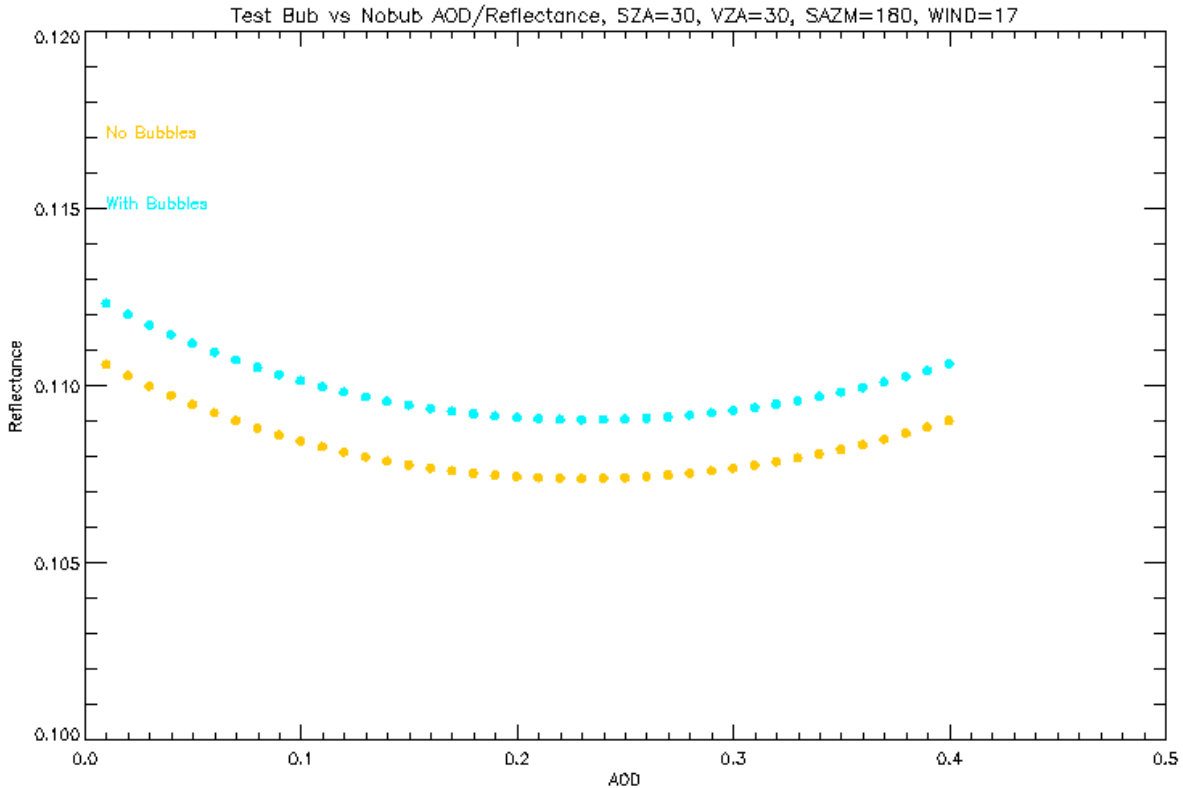

Figure 16. This plot has reflectance plotted against AOD. The viewing geometry is labeled in the plot title, and the wind speed is constant at 17 m/s. Notice the restricted range of the y-axis.

Based on Figures 12-15, it is evident that at low wind speeds there is no significant impact from ocean bubbles; however, as wind speeds increase so does ΔAOD. The impact becomes more significant once wind speeds are above 10 m/s as ΔAOD values begin to surpass 0.01 and increase exponentially. While surface wind speeds of this magnitude do not occur on a global scale, (average global wind speed is around 6-

7m/s), for regions with high wind speed such as the ESOA region, the impacts of ocean bubbles on the satellite retrieved AOD values can be significant.

3.4.4 Fixed SZA and AODbub, varied SAZM

Equation 10 shows that varying the relative azimuth angle (the difference between SAZM and VAZM) changes the glint angle. In this study, VAZM is held constant at 0 degrees, therefore varying the SAZM will change the relative azimuth angle. Figure 17 shows the progression of changing the SAZM from 0 to 180 degrees. The starting AOD value was held constant at 0.1.
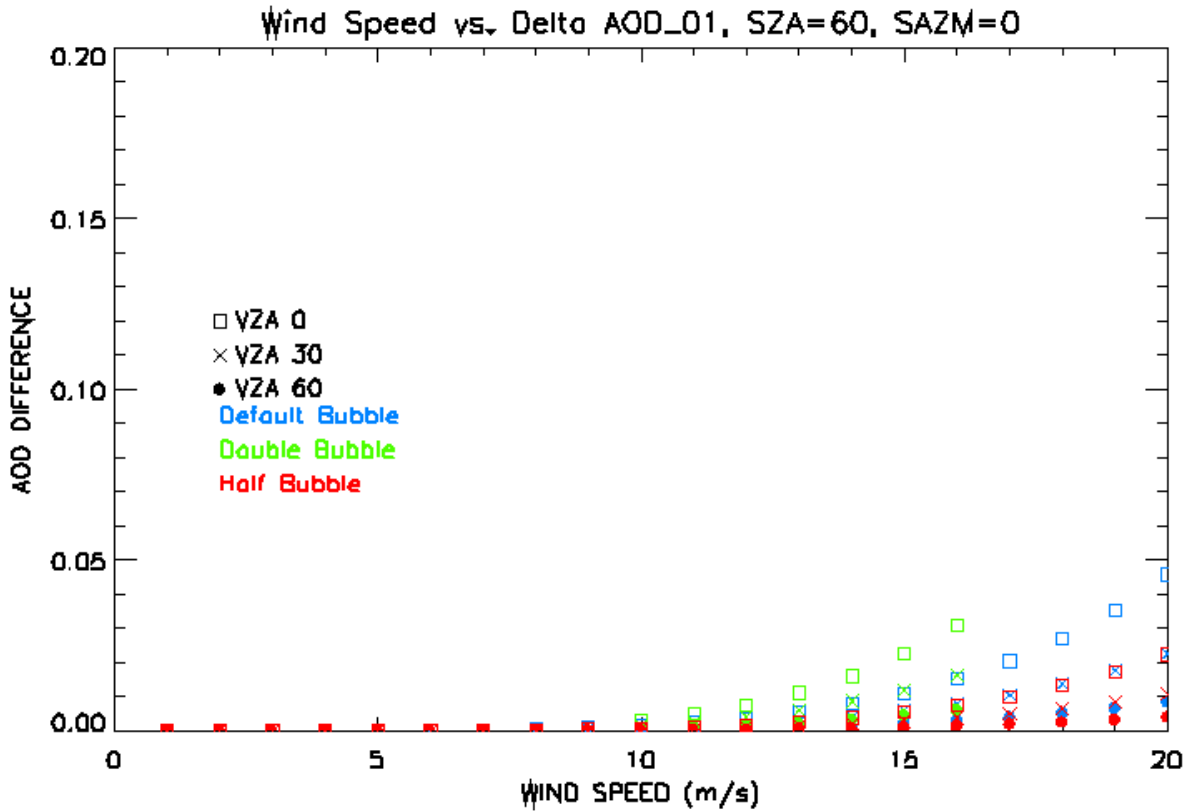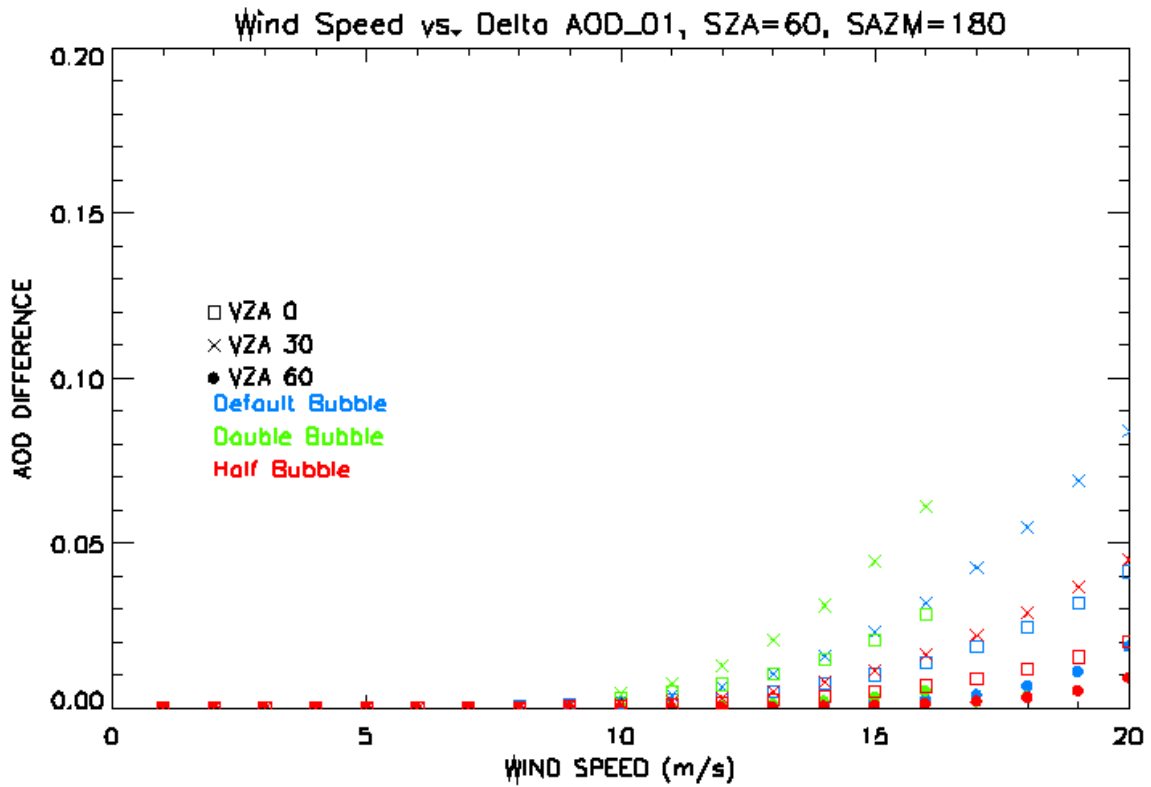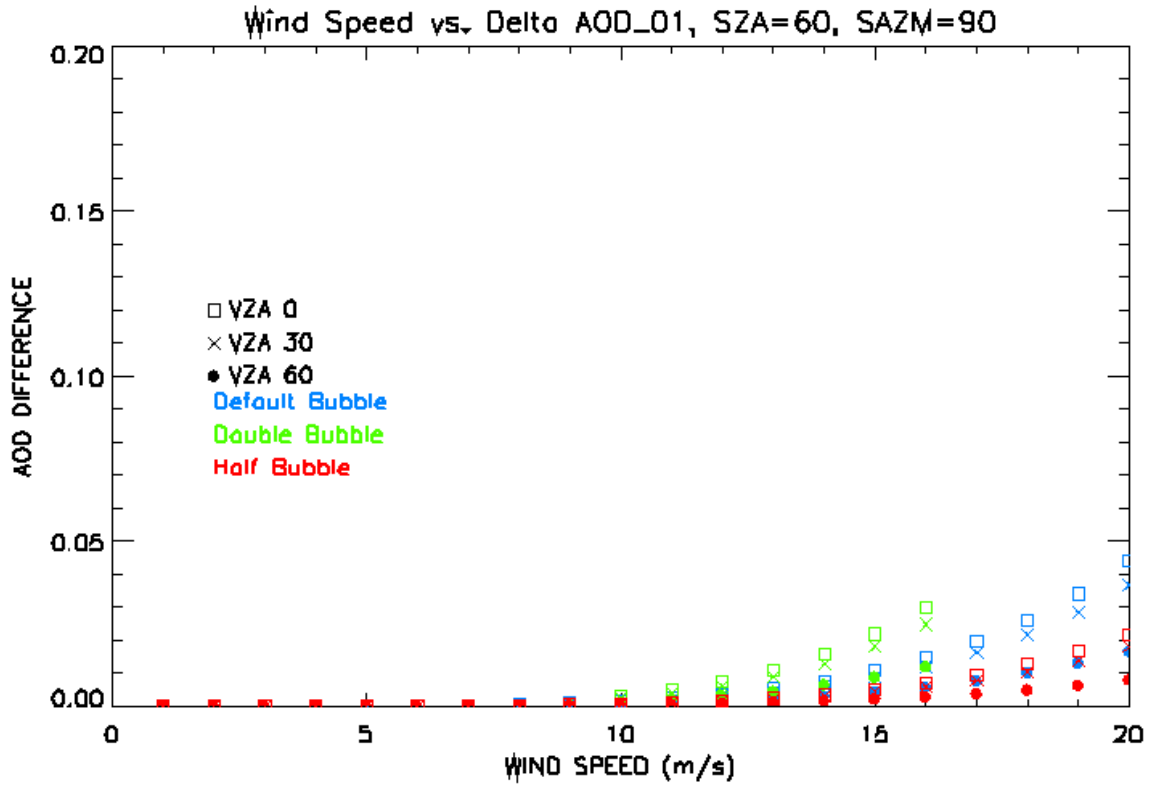
Figure 17. ΔAOD plotted as a function of wind speed at a constant SZA of 60 degrees and starting AOD value of 0.1. top) SAZM=0°, middle) SAZM=90°, bottom) SAZM=180°

As SAZM increases, ΔAOD increases for certain viewing geometries. This is
likely due to contributions from sun glint, which is more pronounced when the relative
azimuth angle is 180 degrees. This will in turn have an effect on the reflectance output.
Figure 18 shows the average ΔAOD from Fig. 17 as a function of wind speed.
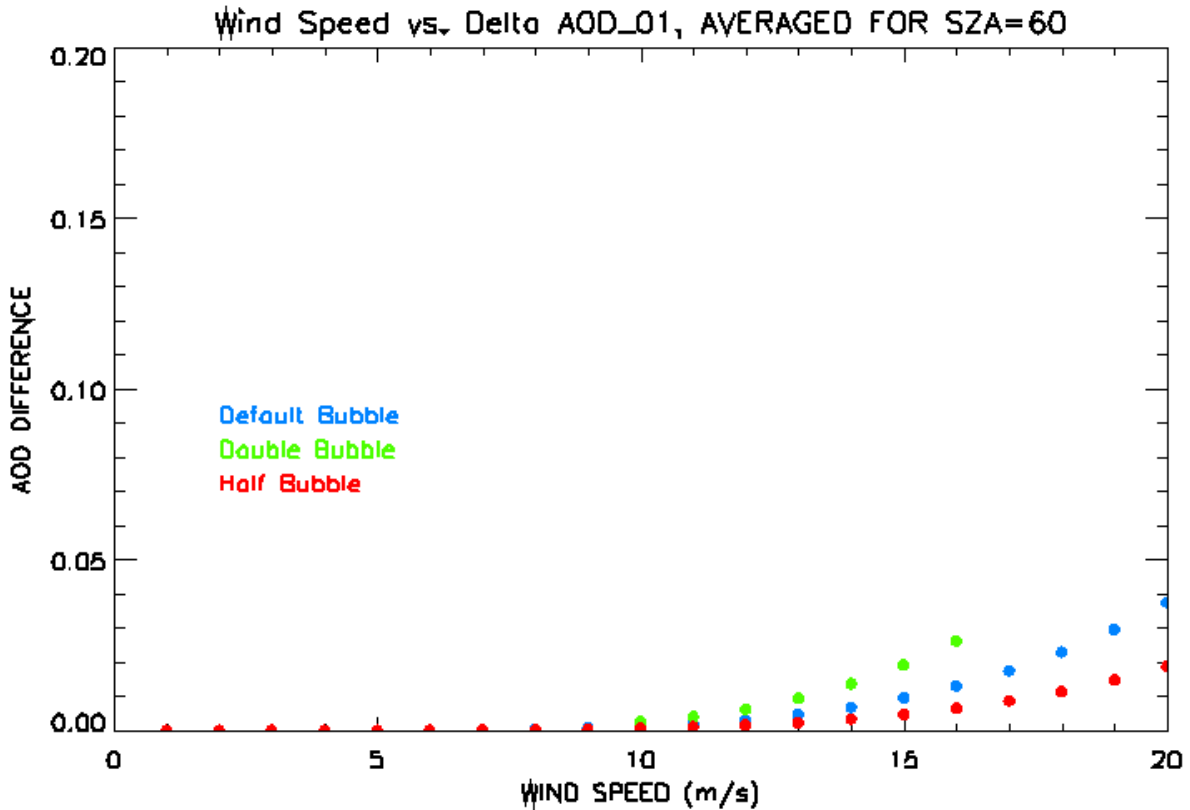
Figure 18. The average ΔAOD as a function of wind speed for solar zenith angle of 60° at a
starting AOD value of 0.1.

This indicates that the impact of ocean bubbles at a SZA of 60° is more apparent
as wind speeds exceed 12 m/s. This wind speed threshold is slightly higher than what
was seen at a SZA of 30°. This reinforces the importance of viewing geometry, as solar
zenith angle, viewing zenith angle, and relative azimuth angle all have an impact on AOD
retrievals.

3.5 Apply Ocean Bubble Correction to the ESOA

It has been shown that, theoretically, ocean bubbles can affect satellite aerosol retrievals under conditions with near surface wind speeds greater than 10-12 m/s. As the last step of this analysis, we study the impact of oceanic bubbles to the ESOA feature detected from MODIS. For this exercise, one year (2009) of Aqua MODIS AOD and AMSR-E wind speed data are used. For each day, AMSR-E wind speed (Fig. 19a), Gridded Aqua MODIS AOD (Fig. 19b), solar zenith, viewing zenith, relative azimuth angels data are constructed at a 1x1 degree (Lat/Lon) resolution. Based on the LUTs constructed in previous section, yearly averaged changes in retrieved AOD due to bubbles (ΔAOD) are also calculated (Fig. 19c). Lastly, ΔAOD is subtracted from the data in Fig 19b to created corrected AOD due to the impact of ocean bubbles (Fig. 19d).

Figure 19a is a plot of the average global wind speed for the year 2009. Notice a high wind speed band is found over the high latitude southern oceans, which is consistent with the location of the ESOA feature. Figure 19b is the yearly averaged Aqua MODIS AOD for the latitude range of -70 to -30 degrees. Using the LUTs created in section, the ΔAOD can be estimated with the use of the viewing geometry and wind speed as inputs to the LUTs and through linear interpolations of LUT outputs. The ΔAOD values for the same area as Fig. 19b are shown in Fig. 19c. The ΔAOD can then be subtracted from the Aqua MODIS AOD (Fig. 19b) to evaluate the impact of ocean bubbles. This step is shown in Fig. 19d. An evaluation of Fig. 19c and Fig. 19d suggests that ocean bubbles have a minor effect to the ESOA. It is likely that ESOA is originated from sources other than oceanic bubbles.
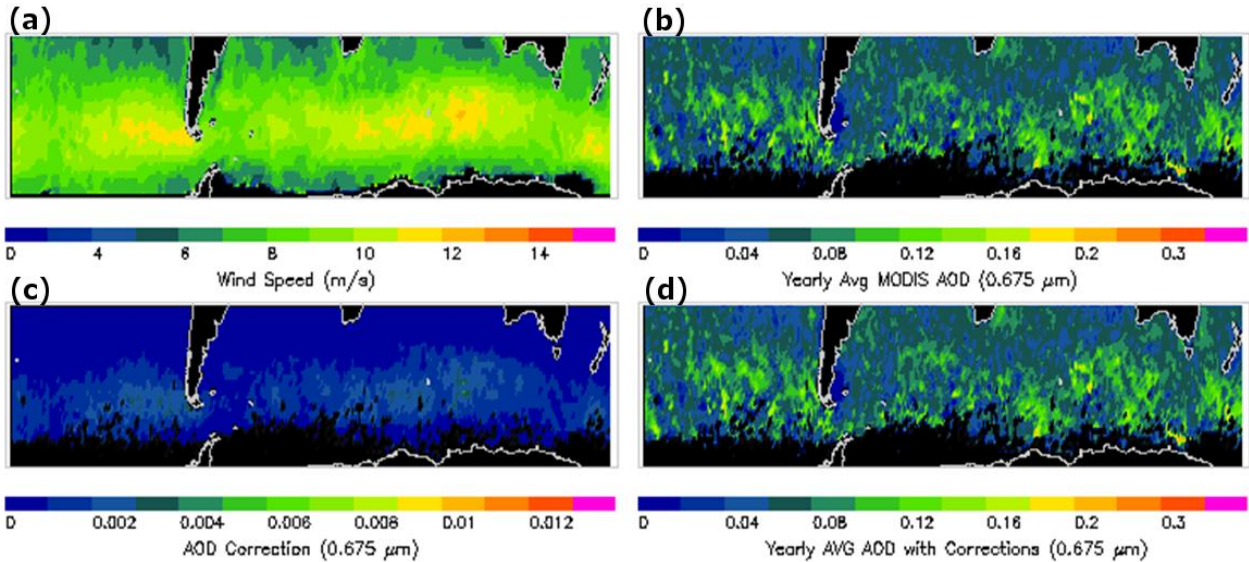
Figure 19. a) Yearly averaged wind speed for 2009 for the latitude range of -30 to -70 degrees. b) yearly averaged AOD for the same region as shown in Figure 19a. c) Corrections to account for ocean bubbles based on the yearly averaged wind speed and viewing geometry. d) New yearly averaged AOD after applying the ocean bubble corrections.

Figure 20 is the percentage change in AOD as a result of ocean bubbles. It is visible that almost all areas sustain an AOD change of less than 10%, with a majority having less than a 4% change in AOD. The average wind speed is not high enough to sustain a large contribution from ocean bubbles.
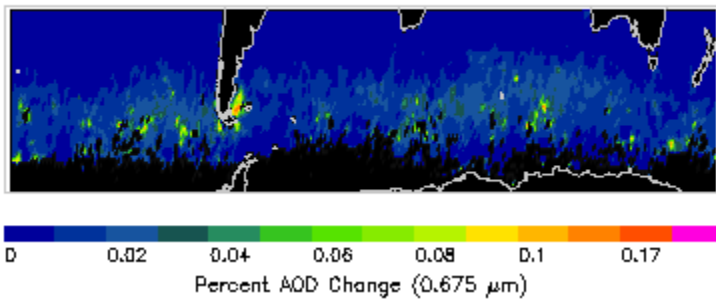

Figure 20. Similar to Fig. 19c, this is AOD correction plotted as a percentage.

Figure 21 is a histogram of the wind speeds in the ESOA region over a full year (2009). Figure 21a is the wind speed measured in the ascending orbit, and Fig. 21b is the data from the descending orbit. Regardless of the ascending or descending orbit, the wind speed spread peaks

38

around 10 m/s, but then decreases exponentially. Therefore the vast majority of overall wind speeds measurements are less than 10 m/s. Each orbit indicates that there are instances where the wind speeds can exceed 15 m/s and even 20 m/s, however there are very few incidents of wind speeds of this magnitude over the course of a year when compared to other wind speed events.

While there are high speed wind events in the ESOA region, when averaged over a year the impact of these events is nullified. This is reason as to why ocean bubbles do not appear to contribute to the ESOA phenomenon.
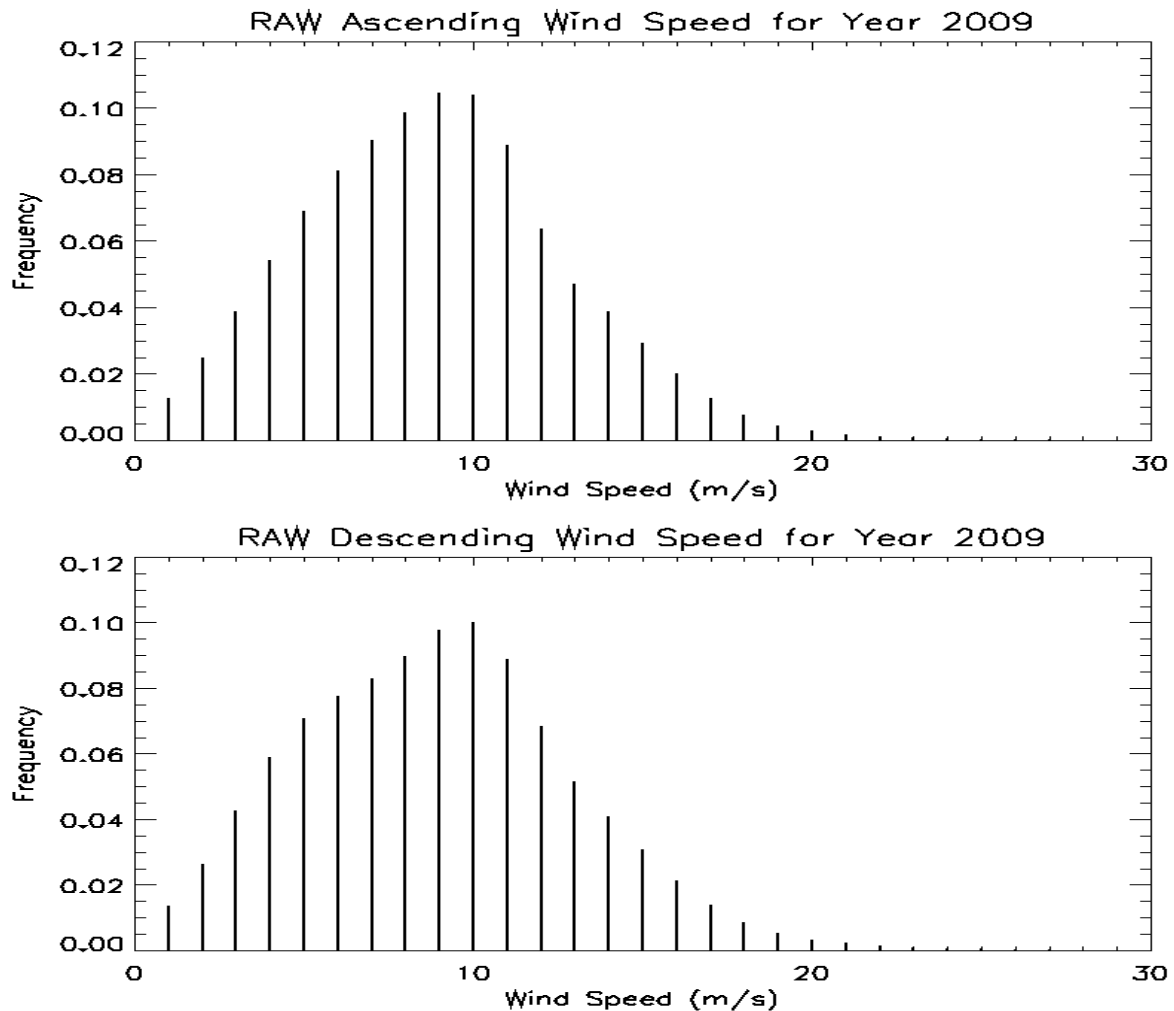

Figure 21. Top histogram: wind speed frequency over a whole year (2009) for the ascending orbit. Bottom histogram: wind speed frequency over the same year for the descending orbit.

CHAPTER IV

CONCLUSIONS

Previous studies have demonstrated the effects of oceanic bubbles on surface reflectance patterns. However, ocean bubble effects have not been related to atmospheric applications such as aerosol retrievals by passive remote sensing techniques. By coupling the HydroLight oceanic radiative transfer model (RTM) with the 6S atmospheric RTM, the effects of ocean bubbles on satellite aerosol measurements are studied.

Our initial investigation, using observed aerosol optical depth, wind speed and satellite radiance data from MAN, AMSR-E, and MODIS, are inconclusive, as the uncertainties in the modeled MODIS radiance are comparable in magnitude with the bubble induced perturbations in TOA radiation. Also, modeled standard atmospheric profiles could differ from observed atmospheric profiles.

A large scale theoretical approach is taken next by varying multiple variables including solar zenith angle, viewing zenith angle, solar azimuth angle, wind speed, and AOD. The bubble-induced uncertainty in AOD value retrieved from passive sensors (ΔAOD) is calculated as functions of satellite viewing geometry, near surface wind speed, and AOD. The wind speed data are included as bubbles are formed by breaking ocean waves, which are a function of wind speed. It is evident that at low wind speeds there is no significant impact from ocean bubbles on AOD retrievals using passive remote sensing techniques. However the impact becomes much more significant at wind speeds above 12 m/s. On average, the global wind speed is around 6-7 m/s, which is too low for ocean bubbles to have a significant effect on the global climate.

However, high wind speeds can be found over regions such as the northern hemisphere storm track, and therefore the impact of ocean bubbles may need to be considered for future satellite aerosol retrievals in such regions.

Finally, the impacts of oceanic bubbles to the ESOA phenomenon are evaluated using one year of MODIS, and AMSR-E data.   It is found that ocean bubbles are not a major contributing factor to the ESOA.

REFERENCES

AMSR data produced by Remote Sensing Systems. Retrieved June 8, 2012. http://www.remss.com/missions/amsre

Crawford, G. B. and D. M. Farmer (1987), On the spatial distribution of ocean bubbles, Journal of Geophysical Research: Oceans, 92, 8231 – 8243.

Czerski, H., M. Twardowski, X. Zhang, and S. Vagle, (2011) Resolving size distributions of bubbles with radii less than 30 μm with optical and acoustical methods, Journal of Geophysical Research, 116, 1 – 13.

D'Arrigo, J. S. (1983), Biological surfactants stabilizing natural microbubbles in aqueous media, Advances in Colloid and Interface Science.

D'Arrigo, J. S., C. Saiz-Jimenez, and N. S. Reimer (1984), Geochemical properties and biochemical composition of the surfactant mixture surrounding natural microbubbles in aqueous media, Journal of Colloid and Interface Science, 100, 96 – 105.

Holben B.N., T.F. Eck, I. Slutsker, D. Tanré, J.P. Buis, A. Setzer, E. Vermote, J.A. Reagan, Y. Kaufman, T. Nakajima, F. Lavenu, I. Jankowiak, and A. Smirnov (1998), AERONET - A federated instrument network and data archive for aerosol characterization, Rem. Sens. Environ., 66, 1 – 16.

Knobelspiesse, K. D., C. Pietras, and G. S. Forgion (2003), Sun-pointing Error Correction for Sea Deployment of the MICROTOPS II Handheld Sun Photometer, Journal of Atmospheric and Oceanic Technology, 20, 767 – 771.

Koepke, P. (1984), Effective Reflectance of Oceanic Whitecaps, Applied Optics, 23 (11), 1816 – 1824.

Lamarre, E. and W. K. Melville (1991), Air entrainment and dissipation in breaking waves, Nature, 351, 469 – 472.

Mobley, C. D., L. K. Sundman (2012), HydroLight 5.1 EcoLight 5.1 Users' Guide, Sequoia Scientific, Inc., Bellevue, 102 p.

MODIS Collection 5 Dark Target Aerosol Products. Retrieved March 1, 2013. http://ladsweb.nascom.nasa.gov/

Morel A, and S. Bélanger (2006), Improved detection of turbid waters from ocean color sensor information, Remote Sensing of Environment, 102, 237 – 249.

Porter, J. N., M. Miller, C. Pietras, and C. Motell (2001), Ship-based Sun Photometer Measurements Using Microtops Sun Photometer, Journal of Atmospheric and Oceanic Technology, 18, 765 – 774.

Remer L. A., Y. J. Kaufman, D. Tanré, S. Mattoo, D. A. Chu, J. V. Martins, R. R Li, C. Ichoku, R. C. Levy, R. G. Kleidman, T. F. Eck, E. Vermote, and B. N. Holben (2005), The MODIS aerosol algorithms, products, and validation, Journal of Atmospheric Sciences – Special Edition, 62, 947 – 973.

Shi Y., J. Zhang, J. S. Reid, B. Holben, E. J. Hyer, and C. Curtis (2010), An analysis of the Collection 5 MODIS over-ocean aerosol optical depth product for its implication in aerosol assimilation, Atmos. Chem. Phys. Discuss., 10, 20239 – 20265.

Smirnov, A., B. N. Holben, D. M. Giles, I. Slutsker, N. T. O'Neill, T. F. Eck, A. Macke, P. Croot, Y. Courcoux, S. M. Sakerin, T. J. Smyth, T. Zielinski, G. Zibordi, J. I. Goes, M. J. Harvey, P. K. Quinn, N. B. Nelson, V. F. Radionov, C. M. Duarte, R. Losno, J. Sciare, K. J. Voss, S. Kinne, N. R. Nalli, E. Joseph, K. Krishna Moorthy, D. S. Covert, S. K. Gulev, G. Milinevsky, P. Larouche, S. Belanger, E. Horne, M. Chin, L. A. Remer, R. A. Kahn, J. S. Reid, M. Schulz, C. L. Heald, J. Zhang, K. Lapina, R. G. Kleidman, J. Griesfeller, B. J. Gaitley, Q. Tan, and T. L. Diehl (2011), Maritime Aerosol Network as a component of AERONET − first result and comparison with global aerosol models and satellite retrievals, Atmos Meas. Tech, 4, 583 − 597.

Thorpe, S. A. (1982), On the clouds of bubbles formed by breaking wind-waves in deep water, and their role in air − sea gas transfer, Phil. Trans. R. Soc. Lond. Series A, 304, 155 − 210.

Thorpe, S. A. (1986), Measurements with an automatically recording inverted echo sounder; ARIES and the bubble clouds, Journal of Physical Oceanography, 16, 1462 − 1478.

Thorpe, S. A. and P. N. Humphries (1980), Bubbles and breaking waves, Nature, 283, 463 − 465.

Toth T. D., J. Zhang, J. R. Campbell, J. S. Reid, Y. Shi, R. S. Johnson, A. Smirnov, M. A. Vaughan, and D. M. Winker (2013), Investigating enhanced Aqua MODIS aerosol optical depth retrievals over the mid-to-high latitude Southern Oceans through intercomparison with co-located CALIOP, MAN, and AERONET data sets, Journal of Geophysical Research: Atmosperes, 118, 4700 − 4714.

Vermote, E., D. Tanré, J. L. Deuzé, M. Herman, J. J. Morcrette, and S. Y. Kotchenova (2006), Second Simulation of the Satellite Signal in the Solar Spectrum − Vector (6SV) User Guide Version 3, http://6s.ltdri.org/6S_code2_thiner_stuff/6s_ltdri_org_manual.htm

Zhang X., M. Lewis, and B. Johnson (1998), Influence of bubbles on scattering of light in the ocean, Applied Optics, 37 (27), 6525 – 6536.

Zhang X. (2001), Influence of Bubbles on the Water-leaving Reflectance, Dalhousie University, Halifax, 60 – 90.

Zhang X., and M. Lewis (2002) Bubbles and their contribution to the ocean surface albedo, PORSEC 2002 BALI Proceedings, 315 – 319.

Zhang, X., M. Lewis, M. Lee, B. Johnson, and G. Korotaev (2002), The volume Scattering Function of Natural Bubble Populations, Limnol. Oceanogr., 47(5), 1273 – 1282.